

# Illuminating past river incision, sediment source and pathways using luminescence signals of individual feldspar grains (Rangitikei River, New Zealand)

Anne Guyez<sup>1,2</sup>  | Stéphane Bonnet<sup>1</sup> | Tony Reimann<sup>3</sup> | Sébastien Carretier<sup>1</sup> | Jakob Wallinga<sup>2</sup>

<sup>1</sup>GET, Université de Toulouse, IRD, UPS, CNRS, Toulouse, France

<sup>2</sup>Netherlands Centre for Luminescence Dating & Soil Geography and Landscape Group, Wageningen University, Wageningen, The Netherlands

<sup>3</sup>Institute of Geography, University of Cologne, Cologne, Germany

## Correspondence

Anne Guyez, GET, Université de Toulouse, IRD, UPS, CNRS, Toulouse, France.  
Email: anne.guyez@get.omp.eu

## Abstract

Single-grain post-infrared infrared stimulated luminescence (SG-pIRIR) of feldspar has recently been introduced as a method to date Quaternary deposits. The method is particularly appropriate for fluvial deposits that cannot be dated by more conventional quartz optically stimulated luminescence dating and that are heterogeneously bleached (i.e. where only part of the grains is exposed to sufficient light to remove the full luminescence signal). Besides age estimation, single grain equivalent dose ( $D_e$ ) distributions also reflect the variable bleaching degree and origins of grains. Thereby, the SG-pIRIR signal offers a valuable tool to reconstruct sediment pathways. This study builds upon these ideas and develops a dual aspect that combined river terrace dating and SG-pIRIR sediment pathway reconstruction for fluvial deposits in terraces and modern river floodplain along the Rangitikei River (RR), New Zealand. We found that the RR last aggrading phase ( $17.4 \pm 1.9$  ka to  $11.6 \pm 1.5$  ka) was followed by a first phase of fast incision related to knickpoint retreat followed by a steady incision and widening of the RR canyon. The  $D_e$  distribution of fluvial deposits varies accordingly, due in particular to variable input of bedrock particles with saturated pIRIR signal from landsliding of valley flanks. Our study illustrates that the SG-pIRIR approach is well suited to date terraces and shows how SG-pIRIR  $D_e$  distributions provide proxies to reconstruct sediment sources and pathways.

## KEYWORDS

bleaching, dating, fluvial incision, fluvial terrace, geochronology, knickpoint, luminescence, New Zealand, Rangitikei River, riverine landslides, single grain

## 1 | INTRODUCTION

Detrital sediments in fluvial systems are among the best tracers of landscape erosion. As such, modern suspended sediment loads have long been used to estimate catchment-wide erosion rates at the annual to decadal time scale and to evaluate their dependence on potential controlling factors, such as catchment mean elevation, local relief, tectonic uplift or climate (Ahnert, 1970; Carretier et al., 2013; Chen et al., 2021; Fuller et al., 2003; Hinderer et al., 2013; Milliman & Meade, 1983; Milliman & Syvitski, 1992). At a decadal to millennial time scale, cosmogenic radionuclides concentration measured in

fluvial sediments is commonly used to assess basin-wide erosion rates (Binnie et al., 2010; Brown et al., 1995; Carretier et al., 2013; Godard et al., 2014; Granger et al., 1996; Norton et al., 2006; Ouimet et al., 2009; Portenga & Bierman, 2011; Wittmann & von Blanckenburg, 2016). Long- and short-term estimates frequently show contrasted erosion rates due, for example, to the inability of gauging data to correctly incorporate erosion due to high-magnitude, low-frequency events (centennial floods), to transient storage and long transfer time in floodplains (Covault et al., 2013; Guerit et al., 2016; Kirchner et al., 2001), to recent changes in erosion rate—for example in response to human activities (Chen et al., 2021; Kemp et al., 2020;

This is an open access article under the terms of the Creative Commons Attribution-NonCommercial License, which permits use, distribution and reproduction in any medium, provided the original work is properly cited and is not used for commercial purposes.

© 2022 The Authors. *Earth Surface Processes and Landforms* published by John Wiley & Sons Ltd.

Milliman & Syvitski, 1992) or to geomorphological systems in a transient state (Mudd, 2017). In addition to these approaches, methods of provenance analysis of fluvial sediments can provide complementary information on their sources and pathways. A whole family of tracers can be used, as long as they are characteristic of a particular area of the upstream catchment (Clift et al., 2006; Galy & France-Lanord, 2001; Garzanti et al., 2007; Kuhlemann et al., 2001; Lupker et al., 2012; Sawakuchi et al., 2018; Stock et al., 2006).

In recent years, several studies have proposed using the natural luminescence of minerals for tracing earth surface processes (Gray et al., 2019). Luminescence signals are widely used to date deposits (optically stimulated luminescence dating: Huntley et al., 1985) but present many distinctive features that make them interesting tracers for studying fluvial sediment pathways and dynamics (see reviews of Brown, 2020 and Gray et al., 2019). The method makes use of natural luminescence signals of feldspar or quartz grains, minerals usually

abundant in fluvial deposits. A unique feature of the method is that it uses intrinsic properties of the mineral grains themselves (i.e. every grain is a potential tracer, providing major advantages in terms of tracer dilution and analytical limits; Reimann et al., 2015). Major efforts have been made to test the power of luminescence data to better constrain geomorphic processes, by providing innovative data regarding the exhumation of rocks (Biswas et al., 2018; Guralnik et al., 2013, 2015; Herman et al., 2010; King et al., 2016), bedrock-surface exposure (Lehmann et al., 2018; Sohbaty et al., 2012, 2018), soil formation and erosion (Furbish et al., 2018; Gray et al., 2020; Kristensen et al., 2015; Reimann et al., 2017; Román-Sánchez et al., 2019a,b), sediment provenance (Haddadchi et al., 2016; Sawakuchi et al., 2018), fluvial sediment transport (Bonnet et al., 2019; Chamberlain & Wallinga, 2019; Gray & Mahan, 2015; Gray et al., 2017, 2018; McGuire & Rhodes, 2015a,b) and coastal sediment transport (Liu et al., 2009; Reimann et al., 2015).

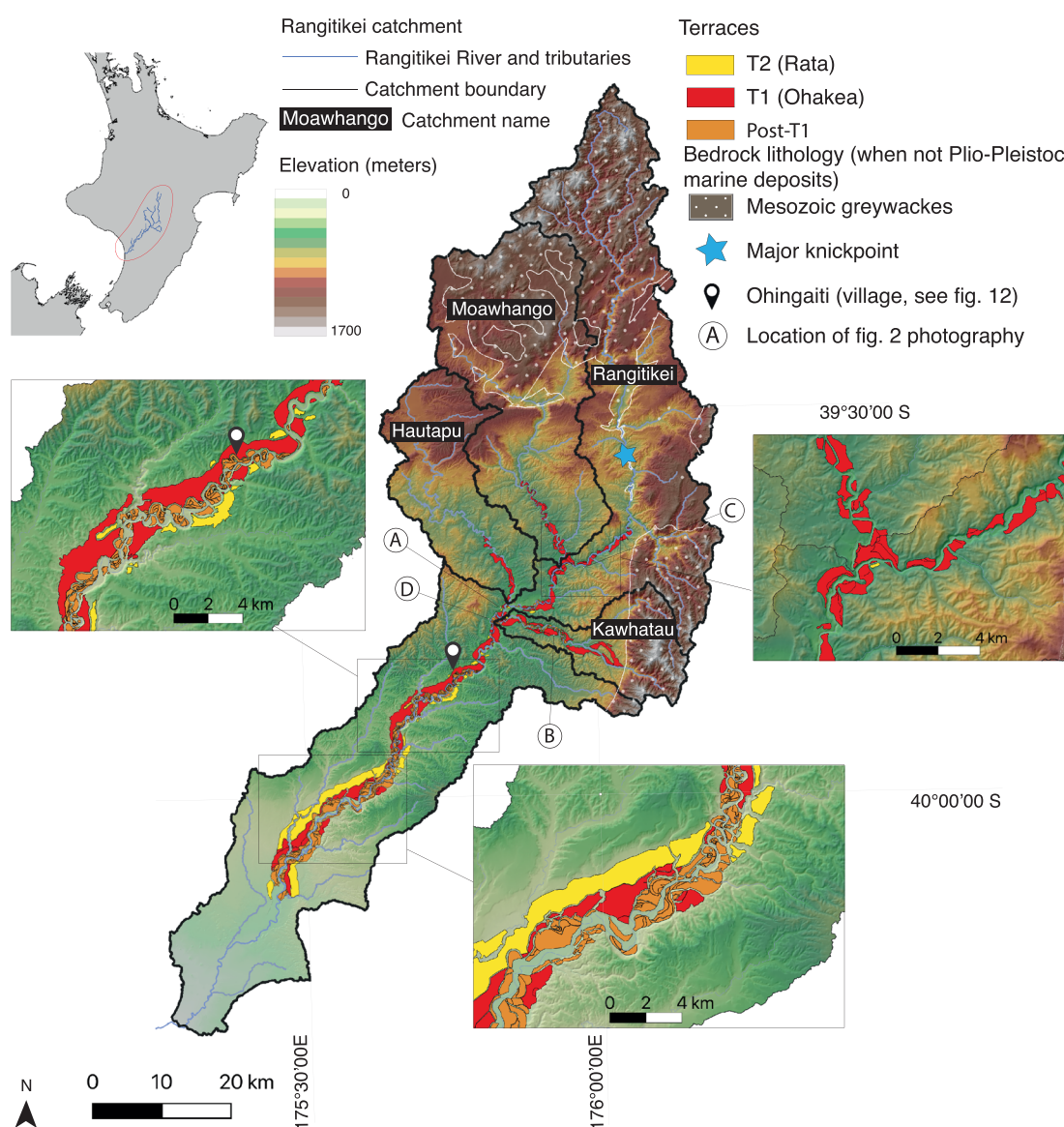


**FIGURE 1** Digital elevation model (DEM) of the southern North Island of New Zealand showing the Rangitikei catchment and its terraces: T2 (yellow), T1 (red) and post-T1 (orange). Bedrock consists of Plio-Pleistocene marine deposits of the Wanganui basin, overlying Mesozoic greywackes that outcrop in headwaters (solid white circles). Contours of sub-catchments of three main tributaries of the Rangitikei River are highlighted, the Moawhango, Hautapu and Kawhatau rivers. Blue star shows the location of the main knickpoint of the Rangitikei River, which delineates an upstream domain where the modern channel is not incised into terrace T1 (see also Figure 4)

Our study adds to this emerging field and presents an innovative way to use equivalent dose ( $D_e$ ) distributions of sand-sized feldspar grains, from modern fluvial sediments and terraces, to reconstruct changes in erosion and transport processes in time. We use post-infrared infrared stimulated luminescence (pIRIR; Thomsen et al., 2008) signals of individual potassium-rich feldspar grains (single-grain pIRIR; Reimann et al., 2012). We focus on the Rangitikei River (RR), New Zealand (NZ), building on a previous study by Bonnet et al. (2019), who already showed that the variability of sediment luminescence signals in this river is controlled by its geomorphic dynamics. Here, SG-pIRIR is used first for dating Late Pleistocene and Holocene terraces, and for reconstructing fluvial incision and valley widening. Then, we consider the SG  $D_e$  distributions as a proxy for geomorphic processes in the fluvial system through time. Our study illustrates how feldspar SG-pIRIR  $D_e$  distributions can identify past and present sediment sources and pathways.

## 2 | RANGITIKEI RIVER, NEW ZEALAND

The  $\sim 3200 \text{ km}^2$  catchment of the Rangitikei is located in the North Island of NZ (Figure 1). Except for the headwaters of the catchment where the bedrock is made up of Mesozoic greywackes, most of the catchment lies on an  $\sim 4.5 \text{ km}$ -thick sequence of Plio-Pleistocene shallow marine deposits (Wanganui basin: Kamp et al., 1998), gently sloping southward. The current exposure of these deposits is the result of partial inversion and uplift of the Wanganui basin since 1–2 Ma (Litchfield & Berryman, 2006), the older units being observed to the North where Quaternary uplift rates reach  $1.5\text{--}2.0 \text{ mm yr}^{-1}$  (Litchfield & Berryman, 2006; Pillans, 1990). A sequence of 750 m of

mudstone to quartzo-feldspathic sandstones (with minor limestones and tephra layers) is currently exposed along the Rangitikei Valley (Journeaux et al., 1996) and constitutes the bedrock of the area. These rocks are weak but cohesive (Rees et al., 2020) and form 100 m-high cliffs with vertical faces along the Rangitikei canyon (Figure 2). During the Pleistocene, the emergence of the land now corresponding to the Rangitikei catchment area and surroundings led to intense erosion of the uppermost deposits of the Wanganui basin, with estimates from mudstone porosity indicating as much as 1–2 km of exhumation (Pulford & Stern, 2004). The sustained competition between uplift and erosion resulted in the development of the current topography, driven by incision of the RR and tributaries. Three main tributaries connect with the RR over a short distance of  $\sim 20 \text{ km}$  in the central part of the RR course (between  $\sim 120$  and  $140 \text{ km}$  from river mouth): the Moawhango, Hautapu and Kawhatau River (KR; Figure 1). Then, downstream of the RR and KR junction, the RR forms a long corridor with connection of only some minor tributaries.

Long-term incision of the RR has been interrupted by periods of climate-driven fluvial aggradation, as testified by sequences of fill terraces (Litchfield & Berryman, 2005; Milne, 1973; Pillans, 1991). The most recent terrace, T1 (also known as Ohakea terrace in NZ stratigraphy; Milne, 1973), is remarkably well preserved along the RR (Figure 2) and its main tributaries. Relicts of T1 threads form a wide corridor that widens gradually downstream (Bonnet et al., 2019) and numerous traces of palaeo-channels at its surface testify to a braided fluvial style (Figure 2A; Bonnet et al., 2019; Milne, 1973; Pillans et al., 1993). Terrace T1 deposits generally consist of a 10–15 m-thick layer of conglomerates, sitting on a bedrock strath surface, marking a major episode of aggradation between 30 and 12 ka (see Bonnet

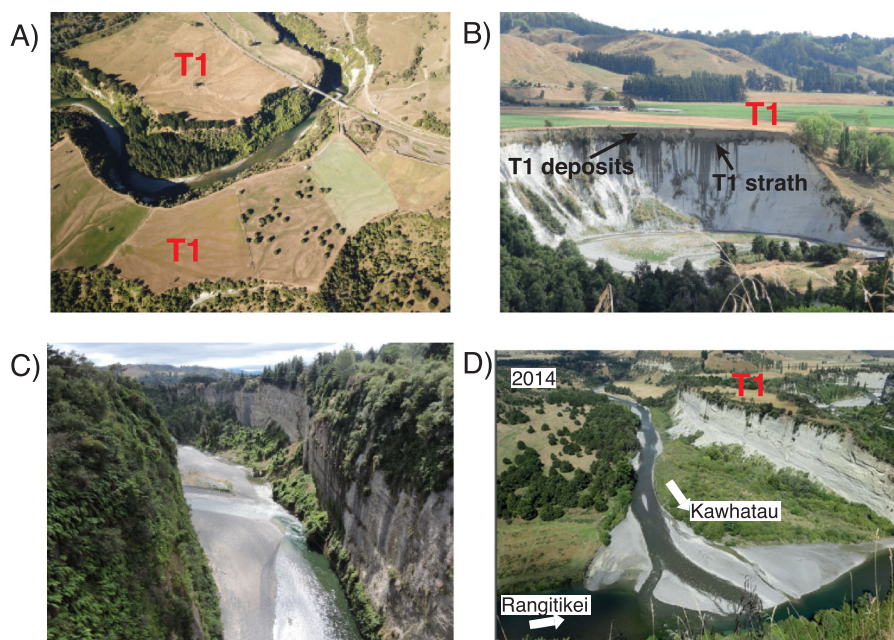


**FIGURE 2** (A) Aerial photograph of upstream section of the Rangitikei River (RR) showing a large paired terrace T1 cut by the canyon of the RR. Note the apparent relicts of the LGM RR braided system at the surface of T1. (B) Photograph of Kawhatau River (KR, see Figure 1) showing terrace T1 at +75 m above modern river level and associated deposits composed of  $\sim 10 \text{ m}$  of T1 conglomerate (dark grey) lying on a strath surface cut into an impermeable light-grey mudstone bedrock. (C) Photograph of the upstream canyon section of the RR close to Taoroa junction (see location in Figure 1). Note the absence of post-T1 terraces. (D) Photograph of the connection of the KR with the RR illustrating the massive input of sediment from the KR at the junction, which creates an alluvial fan in the Rangitikei riverbed. See Figure 1 for location of all photographs



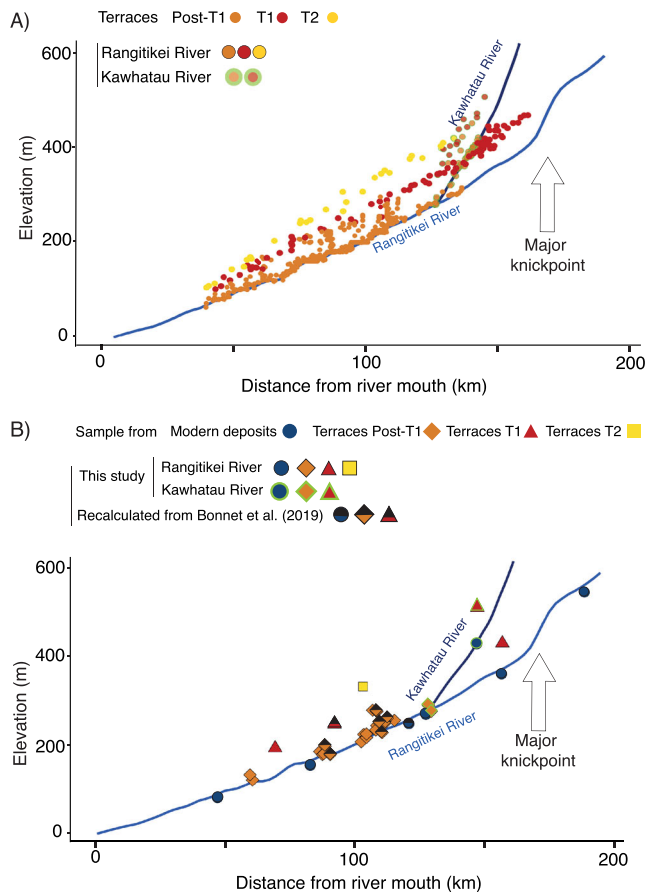


**FIGURE 3** (A) Longitudinal profiles of the Rangitikei and Kawhatau rivers with projection of the T2, T1 and post-T1 terraces. The figure also shows the main knickpoint of the Rangitikei to which a profile defined by remnants of T1 terraces is connected and that delimits an upstream domain where the modern channel is not incised into the T1 surface. Note the absence of post-T1 terraces between this knickpoint and the junction between the Rangitikei and Kawhatau rivers. (B) Longitudinal profiles of the Rangitikei and Kawhatau rivers showing location of samples for luminescence measurements considered in this study

et al., 2019). Terrace T1 and the current RR profiles converge and merge downstream (Figure 3A), a feature documented for many rivers in the North Island of NZ (Litchfield & Berryman, 2006). Upstream, the T1 profile also merges with the modern river profile thanks to a major knickpoint that delineates an upstream part of the profile where the river has not incised into T1 (Figure 3A). The maximum incision of T1 is observed in the central section of the river down the knickpoint, between 50 and 150 km from river mouth (Figures 2B and C and Figure 4), where T1 is now perched at +75 m above the current river bed. There, a long-term ( $\sim 100$  ka time scale) mean incision rate of  $1.5\text{--}2.0\text{ mm yr}^{-1}$  is estimated thanks to age-elevation data for T1 and remnants of two older terraces, T2 and T3 (Bonnet et al., 2019; Litchfield & Berryman, 2006).

Preliminary dating of some cut terraces formed during the Holocene incision phase following abandonment of T1, hereafter referred to as post-T1 terraces (Figure 4B), show that incision was very rapid at first, and then decreased towards recent incision rates of  $\sim 2\text{ mm yr}^{-1}$  (Bonnet et al., 2019). These post-T1 terraces are spatially unevenly distributed, altitudinally as well as longitudinally. Altitudinally, few remnants of post-T1 terraces are found between

relative elevation of +40 m and the T1 thread at +75 m (Bonnet et al., 2019). Longitudinally, post-T1 terraces are absent upstream, in the first 30 km downstream of the main RR knickpoint, where the RR forms a deep canyon (Figures 2C and 4A) and still very little are found until about 60 km from the knickpoint (Figure 3A). It is only some kilometres downstream of the confluence between the RR and the KR that the main sequence of post-T1 terraces is observed (Figures 3A and 4B). There, a total of 300 post-T1 remnants were mapped by Bonnet et al. (2019) over a distance of  $\sim 50$  km. Many correspond to perched abandoned meanders (Figure 4B). In the following, we will expand the preliminary study of Bonnet et al. (2019) by acquiring new single-grain luminescence data for T1, post-T1 and T2 terraces in order to better constrain the Holocene RR incision in space and time and to investigate the additional constraints that the distribution of the luminescence signal may provide on this dynamic. For this purpose, we also acquired luminescence data on modern river deposits.

### 3 | LUMINESCENCE ANALYSIS

#### 3.1 | Background

Luminescence is an intrinsic mineral property of quartz and feldspar. The signal accumulates during burial of the minerals, owing to absorption of ionizing radiation from surrounding rocks or sediments, the mineral itself and cosmic radiation. Ionizing radiation causes trapped charge to build up in structural defects of the crystal over time, until a saturation state occurs with no further accumulation. This trapped charge can be sampled as luminescence through optical or thermal stimulation of the mineral (Aitken, 1998; Wintle, 1999). By comparing the natural luminescence signal to laboratory-induced ones, the absorbed radiation dose can be determined. This quantity is referred to as the equivalent dose ( $D_e$ ). The trapped charges, and thus luminescence signal, are reset when the mineral is exposed to sunlight (bleaching).

#### 3.2 | Sampling

In this study, 28 new samples distributed along the RR (Figure 3B) were analysed for feldspar SG- $\text{pIRIR}$  luminescence. This supplements an existing dataset of nine samples analysed using the same protocol by Bonnet et al. (2019). This total of 37 samples includes (Table 1 and Supplementary Figure S1):

- two samples from fine sandstone bedrock (Wanganui basin deposits);
- one sample from T2 terrace;
- four samples from T1 terrace spread over 88 km, three on the RR and one on the KR (Figure 3B);
- 23 samples from post-T1 terraces distributed over a 70 km stretch downstream of the confluence between the RR and the KR (Figure 3B);
- seven modern samples taken within the floodplain, five on the RR and two on the KR, spread over 142 km. One sample was taken from above the major knickpoint (Figure 3B).

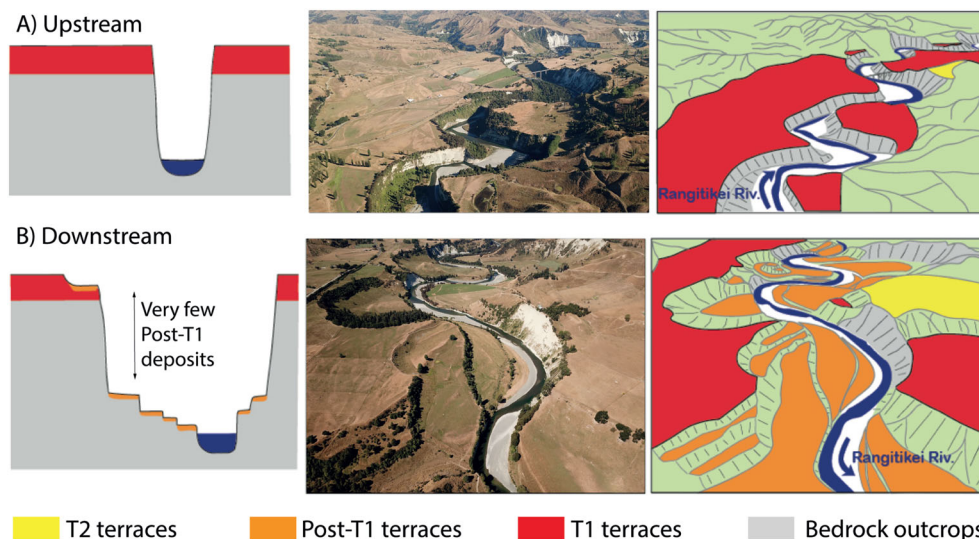


**FIGURE 4** Schematic cross-section (not to scale), photograph and sketch of two different areas along the Rangitikei River (RR). (A) Upstream RR valley section, between its main knickpoint and its connection with the Kawhatau River, illustrating the vertical incision of the RR into terrace T1 and the underlying bedrock, and its canyon shape, without any major flights of post-T1 terraces. (B) Downstream RR valley section, downstream junction with the Kawhatau River, illustrating wandering of the RR with numerous unpaired post-T1 strath terraces, some testifying to perched palaeo-meanders. T1 and T2 terraces are also visible. In both photographs, light grey colours on the canyon flanks are bedrock exposures

See Supplementary Figure S2 and text for details on sample collection.

### 3.3 | Sample preparation and luminescence measurements

All samples were prepared and analysed at the Netherlands Centre for Luminescence dating at Wageningen University (The Netherlands). Luminescence measurements were carried out on feldspar grains (212–250  $\mu\text{m}$ ) using the SG-pIRIR protocol (Reimann et al., 2012), considering 300 individual grains per sample. A combined single-grain infrared stimulated luminescence (IRSL)/pIRIR protocol was employed (Table 2). A pIRIR stimulation temperature of 175°C was chosen as it probes a signal that is reasonably bleachable and not too badly affected by anomalous fading (see Supplementary Figure S3). The number of grains that were accepted for analysis is reported in Table 3 (see online Supplementary Material for details on acceptance criteria). Dose recovery tests were carried out on five samples (see Supplementary Figure S4).

### 3.4 | Apparent age estimation

The SG-pIRIR signals are used to estimate the burial age of deposits, by inferring the palaeodose (= best estimate of burial dose) from the  $D_e$  distribution using appropriate statistical approaches and dividing it by the dose rate (Table 3; see online Supplementary Material). As light exposure of the grains in the fluvial environment is limited, pIRIR signals will only be fully reset in part of the grains. Hence, we determined the palaeodose by applying the bootstrapped Minimum Age Model (BS-MAM; Cunningham & Wallinga, 2012) to the natural SG-pIRIR<sub>175</sub>  $D_e$  distributions. The BS-MAM has been shown to

provide accurate estimates of palaeodose even for heterogeneously bleached samples, provided that the over-dispersion in  $D_e$  distribution of a well-bleached and unmixed sample (sigma-b) is known (Chamberlain et al., 2018). We used here the sigma-b value of  $0.27 \pm 0.10$  determined by Bonnet et al. (2019). In addition, we applied the Central Age Model (CAM; Galbraith et al., 1999) to the full  $D_e$  distribution of each sample to allow comparison with the BS-MAM results. We define the inherited dose as the difference between CAM and BS-MAM palaeodose estimates (residual dose of Chamberlain & Wallinga, 2019) and use it as an indicator for the degree of bleaching.

All palaeodose estimates were calculated using the R Luminescence package (Kreutzer et al., 2012). Note that data for the nine samples of Bonnet et al. (2019) were recalculated using this updated setup (see online Supplementary Material), resulting in slightly different values than originally reported ( $\pm 20\%$  on average), where only the 30% brightest grains were considered. All results of luminescence analyses are reported in Table 3.

### 3.5 | Processes that control luminescence signal distribution

Many processes and factors control the luminescence signal of grains collected in a given geomorphic system (Gray et al., 2019). In fluvial settings, the signals measured include a mix of grains from different sources and transported through different steps that could have increased (during temporary burial) or decreased (when exposed to light during transport or surface exposure) their initial  $D_e$  before their ultimate burial. The SG protocols (Murray & Roberts, 1997 for OSL quartz; Reimann et al., 2012 for pIRIR feldspars) offer data at the smallest resolution—of a unit of transport sediment—necessary to

**TABLE 1** Summary of dataset (samples with an asterisk are from Bonnet et al., 2019)

Origin	Sample	Relative elevation (m above present river)	Elevation (m a.s.l.)	Distance from river mouth (km)	River name	Latitude	Longitude
T2	RO_67	120	335	102.7	Rangitikei	39°52'29.88"S	175°43'55.23"E
T1	RO_57	75	195	68.7	Rangitikei	39°59'30.05"S	175°34'59.90"E
T1	RO_39	75	515	146.9	Kawhatau	39°48'57.13"S	175°57'45.58"E
T1	RO_32	75	434	156.5	Rangitikei	39°41'18.20"S	176°0'28.38"E
T1	RO_04*	75	249	91.7	Rangitikei	39°53'44.14"S	175°40'11.45"E
Post-T1	RO_54	69	281	106.4	Rangitikei	39°51'22.44"S	175°44'23.00"E
Post-T1	RO_40	60	278	108.0	Rangitikei	39°50'35.09"S	175°44'51.31"E
Post-T1	RO_18*	60	280	107.8	Rangitikei	39°50'35.00"S	175°44'51.47"E
Post-T1	RO_13*	38	263	112.0	Rangitikei	39°50'24.06"S	175°46'7.06"E
Post-T1	RO_61	34	134	59.0	Rangitikei	40°0'37.61"S	175°31'40.26"E
Post-T1	RO_47	33	199	88.0	Rangitikei	39°54'43.08"S	175°39'0.29"E
Post-T1	RO_17*	31	253	109.0	Rangitikei	39°50'44.01"S	175°45'14.19"E
Post-T1	RO_41	28	246	108.0	Rangitikei	39°50'45.92"S	175°44'39.34"E
Post-T1	RO_48	23	226	103.0	Rangitikei	39°52'5.78"S	175°43'41.18"E
Post-T1	RO_56	23	258	114.8	Rangitikei	39°49'45.75"S	175°47'16.69"E
Post-T1	RO_45	22	187	86.0	Rangitikei	39°54'59.49"S	175°38'40.64"E
Post-T1	RO_52	22	227	104.0	Rangitikei	39°51'45.09"S	175°44'3.64"E
Post-T1	RO_15*	22	251	111.0	Rangitikei	39°50'31.45"S	175°46'12.88"E
Post-T1	RO_35	20	292	128.0	Kawhatau	39°46'38.46"S	175°49'10.75"E
Post-T1	RO_42	18	236	107.6	Rangitikei	39°50'53.88"S	175°44'41.10"E
Post-T1	RO_46	14	180	87.0	Rangitikei	39°54'48.00"S	175°38'54.98"E
Post-T1	RO_51	14	219	104.0	Rangitikei	39°51'52.09"S	175°44'3.23"E
Post-T1	RO_63	14	122	60.0	Rangitikei	40°0'26.04"S	175°32'43.98"E
Post-T1	RO_10*	12	182	87.5	Rangitikei	39°54'28.16"S	175°39'29.09"E
Post-T1	RO_49	8	209	102.0	Rangitikei	39°52'22.39"S	175°43'29.87"E
Post-T1	RO_36	6.5	278	129.0	Kawhatau	39°46'43.27"S	175°49'12.90"E
Post-T1	RO_01*	6	180	90.0	Rangitikei	39°54'5.12"S	175°40'15.19"E
Post-T1	RO_14*	5	230	110.0	Rangitikei	39°50'33.44"S	175°46'3.38"E
Modern	ROM_01	0	363	156.2	Rangitikei	39°41'13.27"S	176°0'12.70"E
Modern	ROM_04	0	432	146.6	Kawhatau	39°48'35.80"S	175°57'34.96"E
Modern	ROM_06	0	155	82.3	Rangitikei	39°56'3.05"S	175°38'17.07"E
Modern	ROM_07	0	81	46.5	Rangitikei	40°4'33.08"S	175°28'48.39"E
Modern	RO_20*	0	250	120.4	Rangitikei	39°48'32.57"S	175°48'27.85"E
Modern	ROM_02	0	271	127.0	Kawhatau	39°46'36.77"S	175°48'50.98"E
Modern	ROM_05	0	550	188.2	Rangitikei	39°29'17.84"S	176°2'1.20"E

Step	Procedure
i	Laboratory irradiation with regenerative dose (no dose in first SAR cycle)
ii	Preheat at 200°C for 60 s
iii	Single-grain infrared stimulated luminescence (IRSL) at 50°C
iv	Single-grain post infrared-IRSL (pIRIR) stimulation at 175°C
v	Bleaching with IR LEDs for 300 s at 175°C
vi	Laboratory test dose (100 Gy)
vii	Preheat at 200°C for 60 s ('cutheat' identical to preheat; Blair et al., 2005)
viii	Single-grain IRSL stimulation at 50°C
ix	Single-grain pIRIR stimulation at 175°C
x	Bleaching with IR LEDs for 300 s at 175°C
xi	Repeating SAR cycle (i) to (x) for range of regenerative doses (7.5, 15, 30, 60, 120, 240, 0 and 15 Gy)

**TABLE 2** Single-grain pIRIR protocol used in this study

**TABLE 3** Summary of luminescence data (samples with an asterisk are from Bonnet et al., 2019)

	Sample	Number of accepted grains	Saturated grains (%)	Well-bleached grains (%)	Palaeodoses BS-MAM (Gy)	Palaeodoses CAM (Gy)	Residual dose (Gy)	Dose rate (Gy/ka)	Age BS-MAM (ka)
T2	RO_67	124	39	23	112.1 ± 12.3	190.7 ± 8.9	78.6 ± 21.2	3.5 ± 0.2	32.1 ± 3.9
T1	RO_57	81	14	55	57.6 ± 5.6	68.7 ± 3.1	11.1 ± 8.7	3.3 ± 0.2	17.4 ± 1.9
	RO_39	107	21	39	67.6 ± 3.8	116.8 ± 8.4	49.2 ± 12.2	4.6 ± 0.2	14.7 ± 1.0
	RO_32	73	17	50	51.9 ± 3.5	91.2 ± 9.4	39.3 ± 12.9	3.9 ± 0.2	13.4 ± 1.1
	RO_04*	158	7	45	33.8 ± 4.1	57.2 ± 3.5	23.4 ± 7.7	2.9 ± 0.1	11.6 ± 1.5
Post-T1	RO_54	112	11	44	33.8 ± 1.9	67.3 ± 6.2	33.4 ± 8.1	3.7 ± 0.2	9.2 ± 0.7
	RO_40	95	42	26	37.2 ± 2.5	95.2 ± 9.5	58.0 ± 12.0	3.7 ± 0.2	10.1 ± 0.8
	RO_18*	93	16	12	26.8 ± 3.3	95.8 ± 7.3	69.0 ± 10.6	3.5 ± 0.1	7.7 ± 1.0
	RO_13*	88	46	11	38.5 ± 4.7	155.0 ± 10.9	116.5 ± 15.6	3.0 ± 0.2	12.8 ± 1.8
	RO_61	62	67	9	32.2 ± 4.9	162.3 ± 16.3	130.1 ± 21.2	3.5 ± 0.2	9.2 ± 1.5
	RO_47	62	57	10	26.9 ± 4.2	169.0 ± 18.3	142.1 ± 22.4	3.6 ± 0.2	7.5 ± 1.2
	RO_17*	112	40	13	38.4 ± 4.4	146.2 ± 9.3	107.8 ± 13.7	2.9 ± 0.2	13.1 ± 1.7
	RO_41	70	40	12	27.0 ± 4.2	114.7 ± 14.2	87.7 ± 18.4	3.9 ± 0.2	6.9 ± 1.1
	RO_48	73	45	11	22.3 ± 4.5	141.8 ± 20.3	119.4 ± 24.9	4.1 ± 0.2	5.5 ± 1.1
	RO_56	79	34	24	26.0 ± 3.1	82.5 ± 9.7	56.6 ± 12.8	3.9 ± 0.2	6.7 ± 0.9
	RO_45	80	43	8	19.4 ± 3.0	159.3 ± 25.0	139.9 ± 27.9	3.5 ± 0.2	5.5 ± 0.9
	RO_52	51	57	8	25.4 ± 4.4	144.3 ± 25.2	119.0 ± 29.6	3.8 ± 0.2	6.8 ± 1.2
	RO_15*	88	38	13	28.3 ± 3.7	133.5 ± 11.7	105.3 ± 15.4	3.0 ± 0.2	9.5 ± 1.4
	RO_35	147	27	31	34.8 ± 1.9	103.6 ± 10.1	68.8 ± 11.9	4.0 ± 0.2	8.8 ± 0.6
	RO_42	76	41	8	25.7 ± 3.7	143.8 ± 13.3	118.1 ± 17.0	3.8 ± 0.2	6.8 ± 1.0
	RO_46	91	25	22	18.4 ± 2.9	88.4 ± 12.0	69.9 ± 14.9	3.8 ± 0.2	4.8 ± 0.8
	RO_51	68	28	6	3.80 ± 0.8	66.6 ± 9.7	62.9 ± 10.5	2.9 ± 0.2	1.3 ± 0.3
	RO_63	95	36	18	15.7 ± 2.4	77.4 ± 11.1	61.7 ± 13.6	3.3 ± 0.2	4.8 ± 0.8
	RO_10*	67	19	20	15.4 ± 2.2	90.8 ± 12.5	75.4 ± 14.7	3.5 ± 0.2	4.4 ± 0.7
	RO_49	87	17	22	6.6 ± 1.0	63.9 ± 10.1	57.3 ± 11.0	3.5 ± 0.2	1.9 ± 0.3
	RO_36	69	45	8	4.7 ± 0.9	48.1 ± 6.0	43.4 ± 6.9	4.2 ± 0.2	1.1 ± 0.2
	RO_01*	216	39	11	12.8 ± 1.3	157.0 ± 10.9	144.2 ± 12.3	3.2 ± 0.2	4.0 ± 0.5
	RO_14*	122	15	10	5.7 ± 1.0	103.0 ± 8.6	97.2 ± 9.6	3.1 ± 0.2	1.9 ± 0.3
Modern	ROM_01	105	9	6	2.7 ± 0.4	29.8 ± 3.3	27.1 ± 3.7	3.5 ± 0.2	0.8 ± 0.1
	ROM_04	98	47	9	5.3 ± 0.9	121.5 ± 14.9	116.3 ± 15.8	4.2 ± 0.2	1.3 ± 0.2
	ROM_06	87	39	7	2.7 ± 0.5	95.8 ± 12.6	93.2 ± 13.1	3.4 ± 0.2	0.8 ± 0.2
	ROM_07	77	32	5	1.5 ± 0.3	74.8 ± 10.8	73.3 ± 11.0	2.7 ± 0.2	0.6 ± 0.1
	RO_20*	143	6	12	4.3 ± 0.7	67.5 ± 6.5	63.2 ± 7.1	2.5 ± 0.2	1.7 ± 0.3
	ROM_02	97	23	3	5.2 ± 0.8	83.6 ± 10.0	78.4 ± 10.9	3.7 ± 0.2	1.4 ± 0.2
	ROM_05	48	31	9	3.3 ± 1.0	110.8 ± 32.0	107.5 ± 33.0	3.4 ± 0.2	1.0 ± 0.3

decipher the luminescence signal, classify the grains and use it as a geomorphic tool. Yet, when interpreting changes in fluvial dynamics from luminescence signal distributions one should be aware that not all changes may be reflected in the analysed grain-size fraction.

In a typical SG distribution, the grains that give the lowest signal are appointed as well-bleached grains (i.e. grains whose signal was reset before burial). The remaining grains can either: (i) come from direct input of bedrock from valley flanks, valley bottom or hillslope without being bleached prior to their burial; (ii) have been regenerated from older deposits and then remobilized without being fully bleached prior to their reburial; or (iii) have been only partially bleached during transport before burial (Figure 6). Those three types of unbleached or

incompletely bleached grains have an inherited dose at the time of deposition.

### 3.5.1 | Longitudinal partial bleaching

pIRIR signals of grains exposed to sunlight gradually reduce, a process called bleaching. Complete bleaching under subaerial conditions takes a few seconds for quartz and a few minutes for feldspar (Godfrey-Smith et al., 1988; Murray et al., 2012; Smedley & Skirrow, 2020). Subaqueous bleaching is slower due to reduced intensity and light spectrum in water when sediment concentration and turbidity are

high (Berger, 1990; Davies-Colley & Nagels, 2008; Ditlefsen, 1992). Along-stream bleaching (Figure 6) has been documented in natural settings (Jain et al., 2004; McGuire & Rhodes, 2015b; Porat et al., 2001; Stokes et al., 2001) and described as a function of transport distance (Glisanic et al., 2017; Gray et al., 2017; McGuire & Rhodes, 2015b). It is proposed that in absence of along-reach input of freshly eroded material, the amount of trapped charge in minerals decreases downstream. Along-stream bleaching can occur in the suspended load during transport (Berger, 1990; Zhang et al., 2010), with the requirement of a low turbidity that enables light penetration in the water column (Ditlefsen, 1992), or through episodic surface exposure on a sand bar in the floodplains between transport events (Porat et al., 2001), or from a combination of both (McGuire & Rhodes, 2015b).

### 3.5.2 | Lateral input

Grains incorporated into fluvial deposits from lateral input (Figure 6) may contain inherited doses, related to their sources. Mass wasting (including landslide, rockfall and debris flow) is a main process supplying particles from hillsides to rivers in high-relief/tectonically active landscapes (Whipp & Ehlers, 2019). As only a minor fraction of these materials is light exposed during the mass-wasting event, the vast majority of grains entering the river will yield doses reflecting the age of the source material. In such scenarios, the signal measured in fluvial deposits will reflect the diversity of the signal in the rocks themselves (Rittenour, 2008). Therefore, introduction of grains from terraces or bedrock material to the fluvial sediment mix will show up as a specific associated inherited dose in the fluvial deposits, provided that subsequent light exposure is limited.

### 3.5.3 | Regeneration and remobilization of grains

Grains can be temporarily stored in the floodplain. Whether they are completely or partially bleached when buried, their luminescence will increase (regenerate) proportionally to their burial time. Those grains can re-enter the river through lateral input and be incorporated into the transported sediment mix with an inherited dose. Therefore, the luminescence signal measured in the final deposit can also include grains that present an inherited dose gained during their previous burial (Figure 6).

## 3.6 | Grain typology

Following our review of processes that affect the single-grain  $D_e$  distribution of fluvial deposits, we define three types of grains on the basis of their  $D_e$  to use them to trace sources of the particles.

### 3.6.1 | Saturated grains

The luminescence signal of a grain is saturated when it absorbs such a high radiation dose that charge traps are filled and no additional trapped charge can accumulate. We consider the pIRIR<sub>175</sub> signal of a

grain saturated when its sensitivity-corrected natural signal is too elevated to be projected on the laboratory dose response curve (Figure 5C, Table 2), or when the natural signal is above a  $2 \times D_0$  criterion (Wintle & Murray, 2006) (Figure 5B), where  $D_0$  is a characteristic constant in the exponential fitting used in the dose response curve:

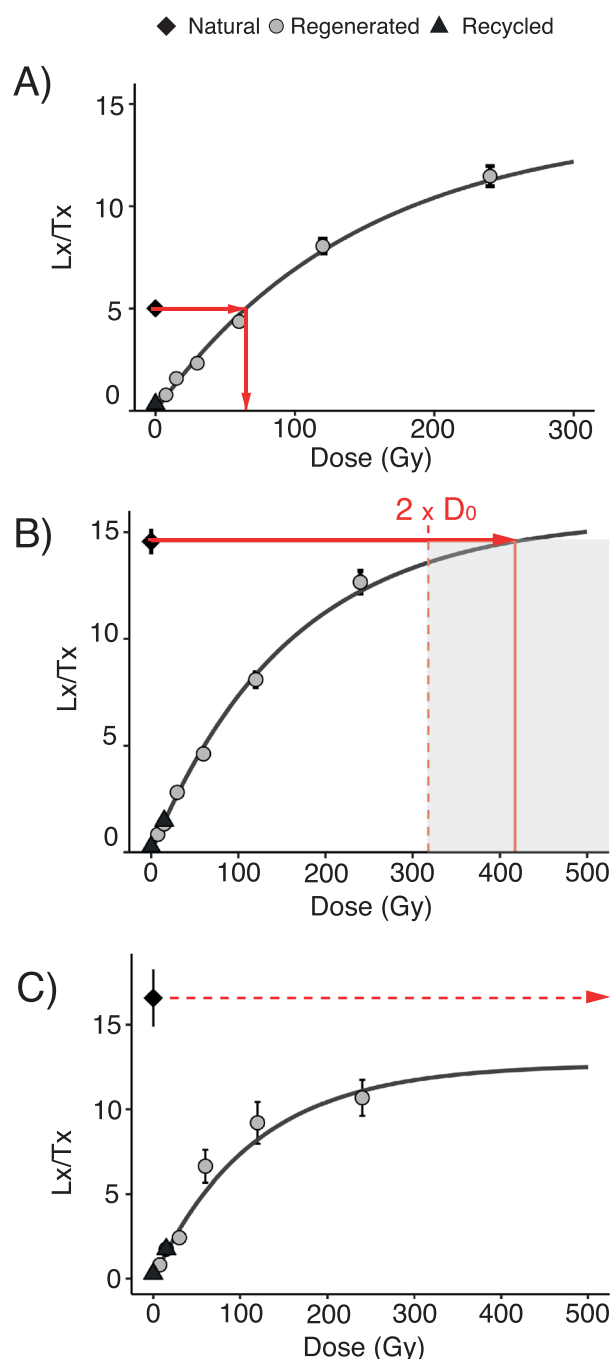


**FIGURE 5** Dose response curves for three grains from sample RO\_41, obtained by fitting a saturating exponential fit to the test dose-corrected regenerated dose points (solid grey circles):  $Lx/Tx = S \times (1 - e^{-D_0/D})$ . (A) The test dose-corrected natural signal (solid diamonds) can be projected onto the dose response curve (red arrows) to determine an equivalent dose  $D_e$ . (B) The test dose-corrected natural signal plots above the saturation threshold of  $2 \times D_0$  (shaded area) and is regarded as saturated in this study. (C) The test dose-corrected natural signal plots above the saturation level and is regarded as saturated



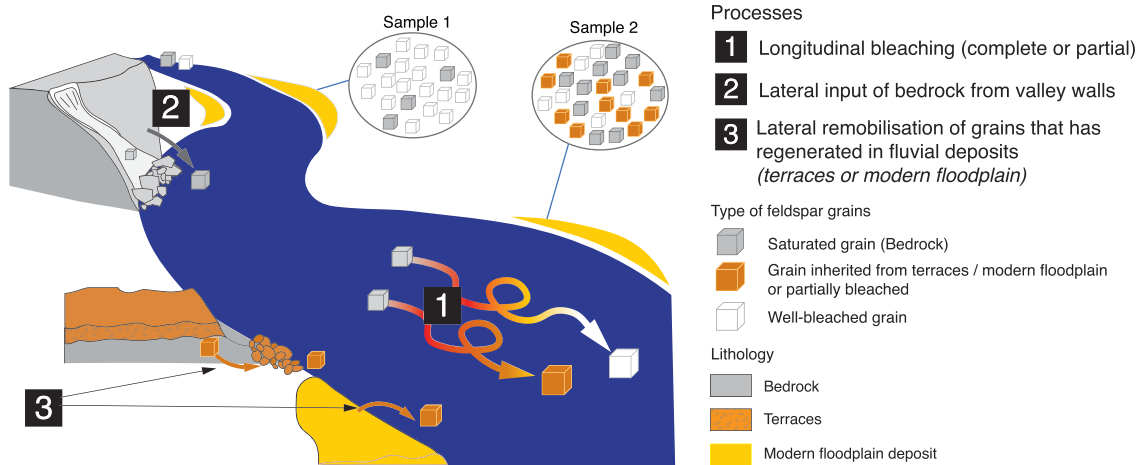


**FIGURE 6** Conceptual scheme describing control processes on the variability of single-grain equivalent dose: (1) longitudinal bleaching during transport, removing all trapped charge (well-bleached grain) or part of it (partially bleached grain); (2) lateral input of bedrock grains with a saturated signal, for example by landsliding of valley walls; (3) lateral remobilization of former fluvial deposits, for example from terraces or modern floodplain. Samples 1 and 2 represent two hypothetical samples from modern alluvial deposits illustrating longitudinal change in the distribution of their single-grain equivalent dose due to these processes

$$Lx/Tx = S \times \left(1 - e^{-\frac{D_0}{D}}\right) \quad (1)$$

with  $Lx/Tx$  the sensitivity-corrected pIRIR signal,  $S$  the luminescence at saturation and  $D$  the regenerative dose.

### 3.6.2 | Well-bleached grains

A grain is defined as well bleached when its  $D_e$  agrees with the BS-MAM estimates from the whole-grain population of the sample, including errors.

### 3.6.3 | Other grains: incompletely bleached and/or with an inherited dose

A grain is considered incompletely bleached and/or with an inherited dose if it is neither saturated nor well bleached. This implies that the total (well-bleached + saturated grains + others) equals 100% of the grains that were accepted for analysis (see online Supplementary Material). Incompletely bleached grains and/or grains with an inherited dose can come from input of saturated grains that have been partially bleached (Figure 6, processes 2 + 1), or from remobilization of regenerated grains potentially partially bleached afterwards (Figure 6, process 3 + eventually 1). In the following, we will focus our analysis on well-bleached and saturated grains as these provide more meaningful information on provenance and transport than the 'other grains'.

## 4 | RESULTS

### 4.1 | Palaeodoses and terrace ages

Apparent burial ages of terrace deposits are  $32.1 \pm 3.9$  ka for the T2 terrace, range from  $11.6 \pm 1.5$  ka to  $17.4 \pm 1.9$  ka for T1 terraces and

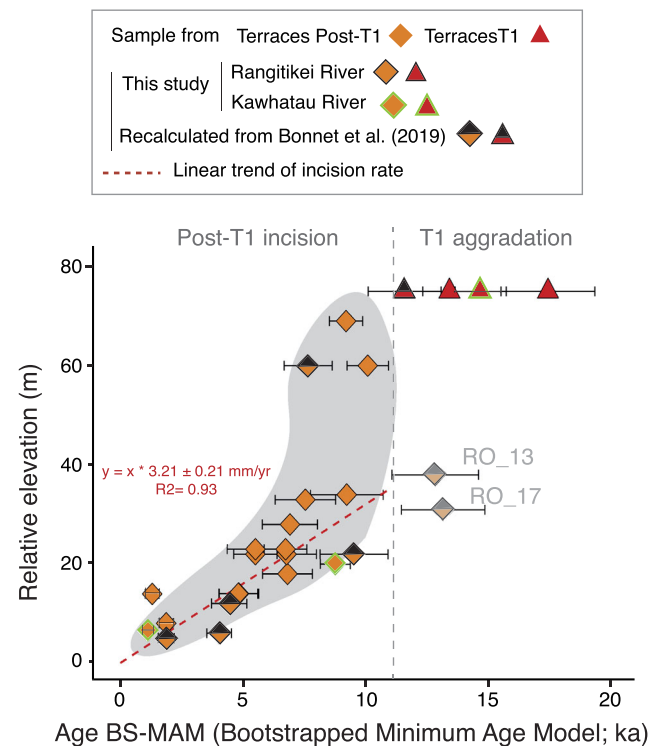


**FIGURE 7** Synthesis of pIRIR BS-MAM single-grain ages for the 4 T1 and 23 post-T1 terraces considered here. Data are plotted as a function of relative elevation of terraces above the present river. Post-T1 terraces RO\_13 and RO\_17 are shown in transparency because their age is considered as anomalous, likely because none of the grains in these samples were bleached at the time of deposition (see text). A linear fit (forced through the origin) on post-T1 data below relative elevation of 40 m indicates a mean incision rate of  $3.21 \pm 0.21$  mm  $\text{yr}^{-1}$  ( $R^2 = 0.93$ )

from  $1.1 \pm 0.2$  ka to  $13.1 \pm 1.7$  ka for post-T1 terraces (Table 3, Figure 7). These ages support previous work by Bonnet et al. (2019), with a change from T1 aggradation to post-T1 incision at  $\sim 11$  ka, followed by a first period of fast incision as evidenced by post-T1

terraces with similar BS-MAM ages but at different relative elevations between +70 and +40 m above the modern channel (Figure 7). A linear fit of ages obtained on post-T1 terraces below relative elevation of  $\sim 40$  m indicates a mean incision rate of  $3.2 \pm 0.2 \text{ mm yr}^{-1}$  ( $R^2 = 0.93$ ), slightly faster than previous estimates by Bonnet et al. (2019).

Data for two post-T1 terraces, RO\_13 and RO\_17, are problematic among the total of 27 T1 and post-T1 ages depicted in Figure 7 because their BS-MAM age appears older than the youngest T1, which is not conceivable with their geomorphic position. We consider these two ages to be anomalous. We will discuss later the likely cause of this age overestimation and will not further consider these two samples for interpreting the RR dynamics.

## 4.2 | Distribution of luminescence signals in terraces and modern deposits

### 4.2.1 | Well-bleached grains

The percentage of well-bleached grains in terraces varies from 6 to 55% (Table 3), the maximum being measured in T1 deposits (39–55%). Post-T1 terraces with the highest proportion of bleached grains (10–44%) are those located near +60 m or below relative elevation of +25 m. Terraces between +25 and +40 m show <10% well-bleached grains. We investigated how this proportion evolved along-stream for subgroups of terrace elevation intervals of 10 m (40/30, 30/20, 20/10 and 10/>0 m; Figure 8). The percentage of well-bleached

grains decreases downward in the two upper subgroups. However, it increases downward in the two lower ones. The percentage of well-bleached grains in modern deposits is quite low, between 2 and 9% (Table 3). Their palaeodoses estimated with the BS-MAM protocol are between  $1.5 \pm 0.3$  and  $4.3 \pm 0.7$  Gy along the RR, and  $5.2 \pm 0.8$  and  $5.3 \pm 0.9$  Gy for the KR (Table 3). Longitudinally (Figure 9A), the modern palaeodoses show a decreasing trend downward from the highest values immediately downstream of the connection of the KR. Upstream of this connection, palaeodoses are lower in the RR but higher in the KR (Figure 9A). Then, it seems that the KR imprints its signature on the modern deposits once connected to the RR. Downstream of this connection, the decrease in modern palaeodoses along the RR likely results from along-stream bleaching during transport.

### 4.2.2 | Inherited doses

We consider here the inherited dose (CAM minus BS-MAM palaeodose estimates), as an additional indicator for estimating the degree of bleaching of samples (Chamberlain & Wallinga, 2019). Among our samples (Table 3), all CAM palaeodose estimates significantly overestimate BS-MAM ones (Figure 7) but to a variable magnitude. The corresponding inherited doses (Figure 10A) are minimal for T1 terraces ( $11.1 \pm 8.7$  Gy to  $49.2 \pm 12.2$  Gy), in contrast to data for post-T1 terraces, whose inherited doses range from  $33.4 \pm 8.1$  Gy to  $144.2 \pm 12.3$  Gy. Maximum inherited doses are observed in post-T1 terraces at mid-elevation between T1 and

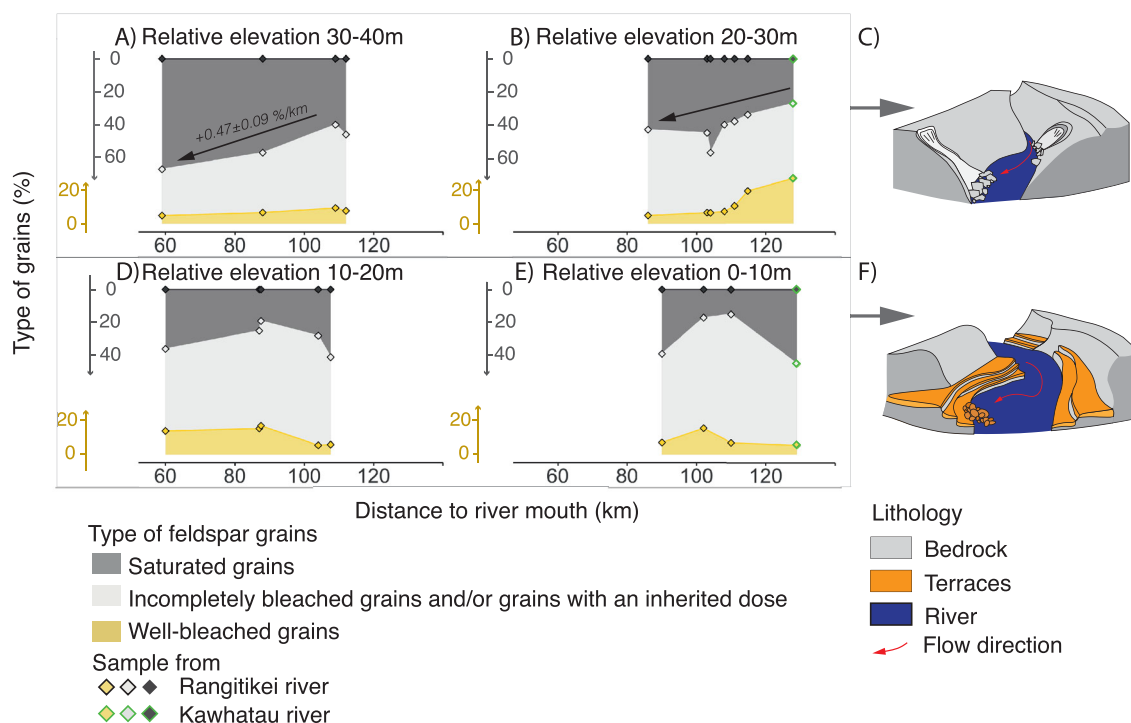
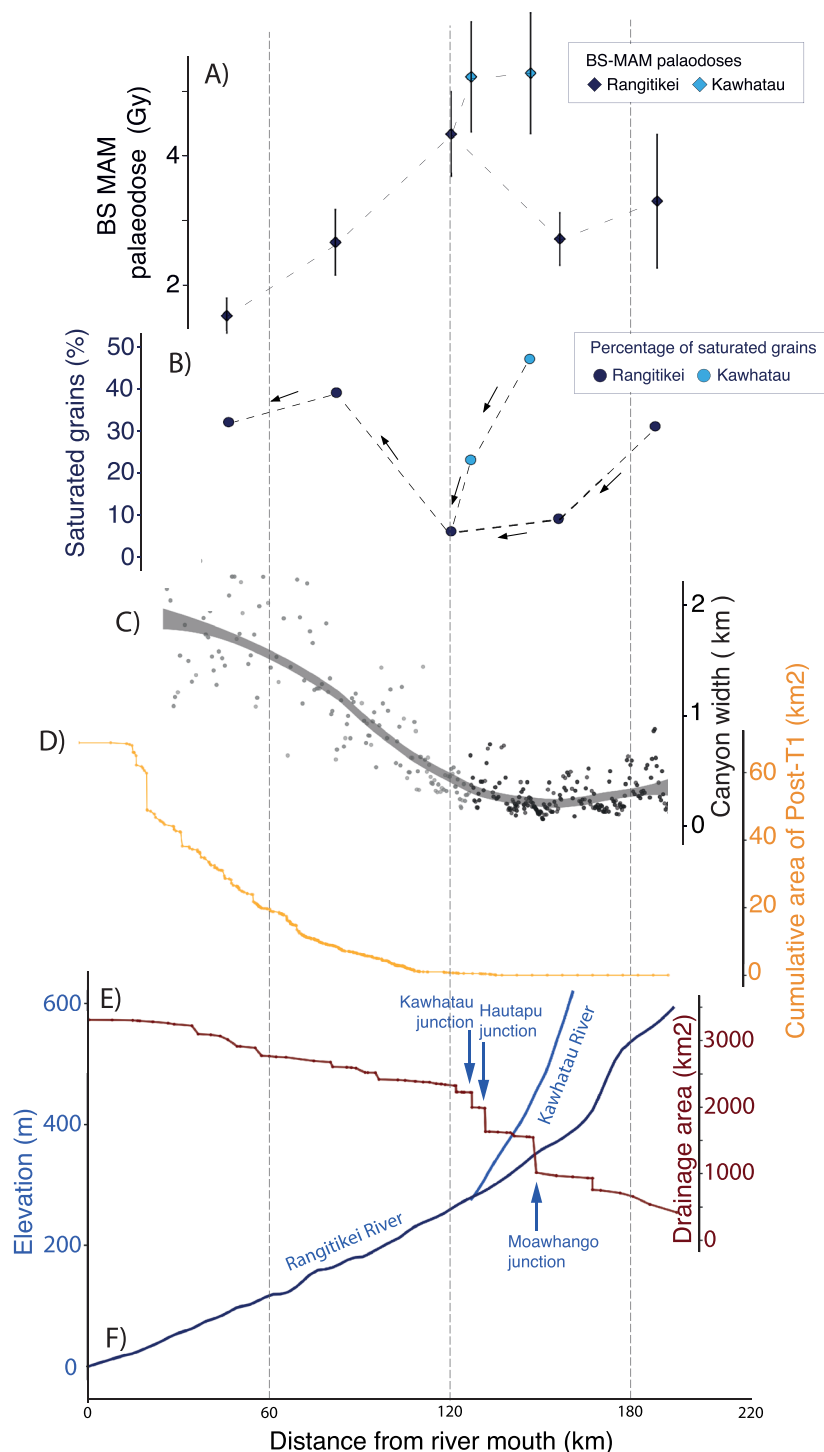


**FIGURE 8** (A, B, D, E) Graphs showing longitudinal evolution of the percentage of different types of grains (saturated, incompletely bleached, well bleached; see main text for definitions) along-stream, according to the specific relative elevation range of post-T1 terraces in four subgroups: (A) 30–40 m; (B) 20–30 m; (D) 10–20 m; and (E) 0–10 m. For the higher post-T1 terraces (in A and B), we observe a downstream increase in saturated grains and a decrease of well-bleached grains, indicating that along-stream input of bedrock material is the dominant process (C). For lower post-T1 terraces (D and E) there is no clear trend, although there may be a slight increase in the percentage of well-bleached grains. This indicates that both longitudinal bleaching and input of bedrock material are important. We attribute this difference to slower incision rates in combination with reduced contact with bedrock cliffs (F, see text)

**FIGURE 9** Along-stream trends for modern river deposits showing (A) palaeodose and (B) percentage of saturated grains in relation to canyon width (C), downward cumulative area of post-T1 terraces (D), drainage area (E) and river profile (F)



the modern river, between  $\sim +40$  m and  $+25$  m (Figure 10A). Below, inherited doses decrease with elevation. The whole pattern of inherited doses with regard to relative elevation defines a boomerang shape (Figure 10A), as already observed by Bonnet et al. (2019).

#### 4.2.3 | Saturated grains

The 35 samples of fluvial sediments all contain saturated grains, with a proportion between 6 and 67% of total measured grains in each sample (Table 3). Among those saturated grains, 85% are of type 'C'

(Figure 5), therefore yielding infinite single-grain ages. The rest (grains of type 'B' in Figure 5) have a mean threshold of 300 Gy, defined by the value  $2 \cdot D_0$ . Complementary to the samples from fluvial deposits, data for two samples taken in the bedrock (Supplementary Table S3) show a very high ratio of saturated grains of 74% (RO\_44) and 89% (RO\_65), while the other grains also have high to very high  $D_e$  values.

The percentage of saturated grains ranges from 7 to 21% for T1 terraces, 11 to 67% for post-T1 terraces (Table 3, Figure 10B) and 6 to 47% for modern sediments (Table 3, Figure 9B). The saturation of post-T1 terraces is maximum for samples between  $+25$  and  $+40$  m, where the majority of grains measured in the samples are saturated

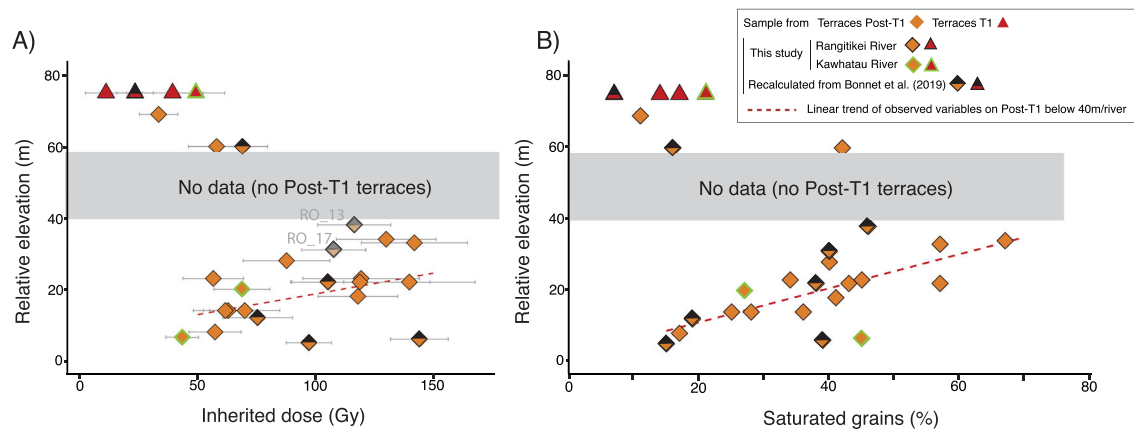


**FIGURE 10** (A) Inherited doses calculated as the difference between CAM and BS-MAM estimates plotted against relative elevation of the terraces above the river. (B) Percentage of saturated grains plotted as a function of relative terrace elevation

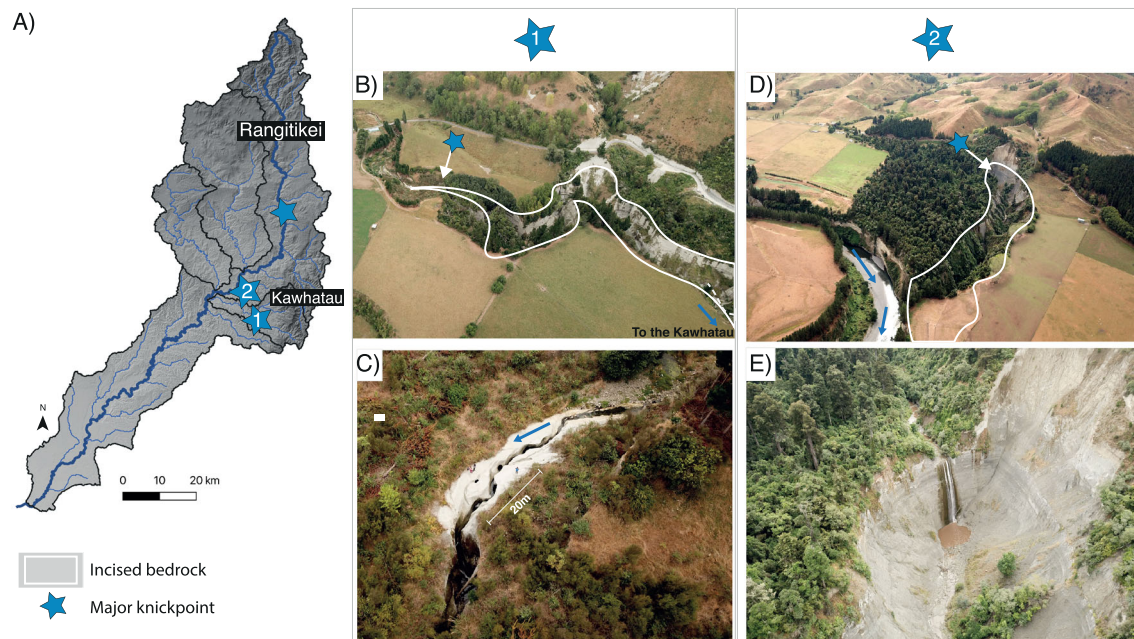


**FIGURE 11** (A) Map of the Rangitikei catchment with blue stars indicating location of some major knickpoints. (B) Aerial photograph of a small tributary of the Kawhatau River where knickpoint #1 is located. (C) Aerial photograph of area around knickpoint #1 showing the river flowing on the bedrock (white colours) and disappearing into narrow gorges (bottom left of the picture) down the knickpoint. (D) Aerial photograph of a small tributary of the Rangitikei River illustrating the area of incised bedrock and the localization of the knickpoint #2. (E) Aerial photograph of knickpoint #2. The waterfall height is approximately 20 m (visual estimates) and has retreated by 720 m from the main RR trunk

(Figure 10B). The percentage of saturated grains tends to be lower for lower terraces and defines a decreasing trend with relative elevation for terraces below +40 m.

Taken all together, post-T1 saturation data do not show any longitudinal tendency. However, some trends emerge for terraces below +40 m when data is split into the elevation subgroups considered previously (Figures 8A–D). Considering separately post-T1 terraces between +30 and +40 m, which are the most saturated (Figure 10B), their percentage of saturated grains increases in the downstream direction by  $0.47 \pm 0.09\% \text{ km}^{-1}$  (Figure 8A;  $R^2 = 0.91$ ). A similar tendency at a comparable rate is observed for the subgroup of terraces below, between +20 and +30 m (Figure 8B), however with a less clear trend ( $0.47 \pm 0.25\% \text{ km}^{-1}$ ;  $R^2 = 0.42$ ). Data do not show any clear trend for the two subgroups of terraces below (Figures 8C and D), the only noticeable point being that their

saturation level is generally lower than that of the two upper subgroups (Figure 10B).

The percentage of saturated grains in modern deposits varies from 6 to 47% (Figure 9B, Table 3) without any clear trend over the total longitudinal distance. Yet, upstream of the RR-KR junction, the percentage of saturation decreases in the two rivers, from 47 and 31% for the KR and RR, respectively, to a minimum of 6% downstream of their junction (Figure 9B). Then, the percentage increases downward to values between 32 and 39%.

## 5 | DISCUSSION

Here, we will first discuss BS-MAM ages in terms of river dynamics with a focus on incision, knickpoint retreat and canyon widening.



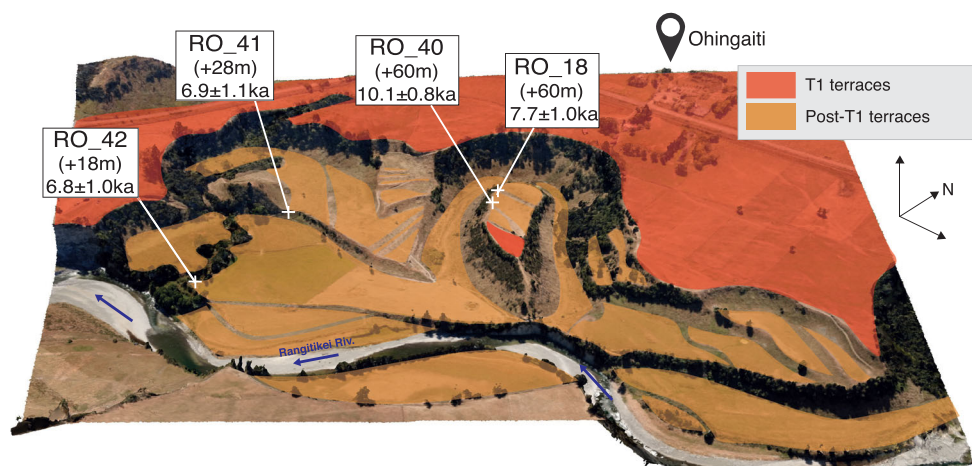


**FIGURE 12** Aerial 3D view of terraces and location of samples close to Ohingaiti village. Two BS-MAM ages of  $10.1 \pm 0.8$  ka (sample RO\_40) and  $7.7 \pm 1.0$  ka (sample RO\_18) have been obtained, respectively, for the bottom and top of a post-T1 terrace whose thread is at +60 m ( $\sim 3$  m of deposits), 15 m below a T1 terrace at +75 m. This indicates  $\sim 18$  m of incision between 11 ka (T1 abandonment) and 10 ka (sample RO\_40), followed by aggradation during  $\sim 2.5$  ka before abandonment of this post-T1 terrace at 7.7 ka (sample RO\_18). 32 and 42 m below, two post-T1 terraces at relative elevation of +28 and +18 m have ages of  $6.9 \pm 1.1$  ka (sample RO\_41) and  $6.8 \pm 1.0$  ka (sample RO\_42). Considering the 32 m of incision between  $7.7 \pm 1.0$  ka and  $6.9 \pm 1.1$  ka (sample RO\_41) or the 42 m between  $7.7 \pm 1.0$  ka and  $6.8 \pm 1.0$  ka (sample RO\_42) and the larger time interval given error bars (2.9 ka: incision between 8.7 and 5.8 ka in both cases) gives a minimum vertical incision rate of  $11 \text{ mm yr}^{-1}$  (sample RO\_41) to  $15 \text{ mm yr}^{-1}$  (sample RO\_42) after abandonment of the post-T1 terrace at +60 m. This rate is  $\sim 40$  to  $45 \text{ mm yr}^{-1}$  considering mean ages. Near here, other dating agrees with this timing, with the BS-MAM age of an upper terrace at +69 m (sample RO\_54) being  $9.2 \pm 0.7$  ka and ages of lower terraces, at elevations of +22 and +23 m, having relatively similar ages to sample RO\_18 (RO\_56:  $6.7 \pm 0.9$  ka at +23 m/river; RO\_52:  $6.8 \pm 1.2$  ka at +22 m/river)

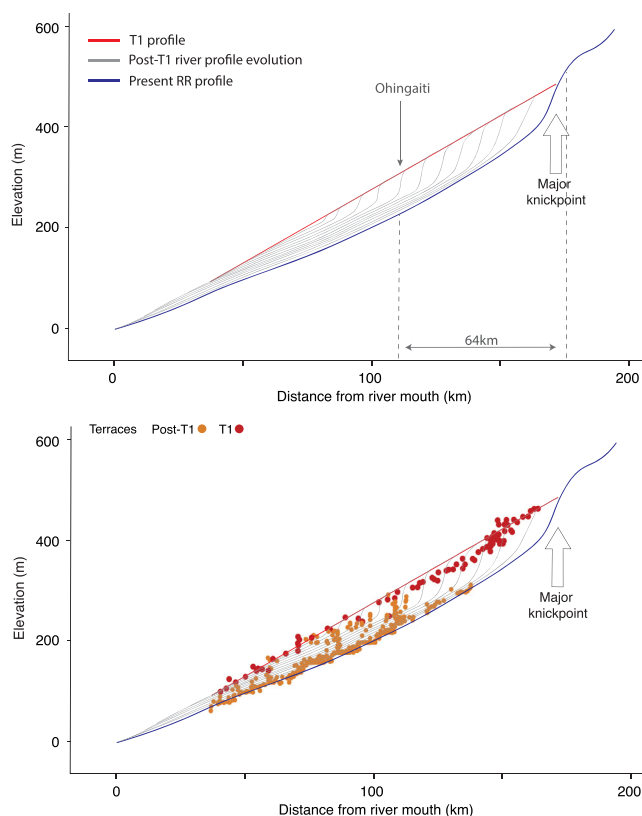


**FIGURE 13** (A) Schematic graph showing the assumed evolution of the Rangitikei River (RR) profile from T1 terraces deposition (red line) until now. Grey thin lines show expected profile evolution during post-T1 incision, involving a first period of knickpoint retreat followed by constant incision. Ohingaiti is located 108 km from the river mouth where we measure the fast incision (see the main text and Figure 12). (B) Same graph including projection of T1 and post-T1 terraces

Then, we will discuss the spatio-temporal variations on sediment sources and pathways inferred from SG-PIRIR  $D_e$  distributions in the context of geomorphic dynamics deduced from dating.

## 5.1 | Incision dynamics

The incision dynamics of the RR is reconstructed using the 28 new age estimates of terraces that complement the preliminary dataset of nine ages of Bonnet et al. (2019). Our new dataset provides the first luminescence dating of a T2 terrace of the RR, of  $32.1 \pm 3.9$  ka, which falls into the age interval estimated for this terrace along the RR and other rivers of the North Island of New Zealand (30–50 ka; see review in Litchfield & Berryman, 2005).

### 5.1.1 | Age of T1 terrace and transition from T1 aggradation to incision

The end of aggradation of T1 is usually considered at  $\sim 15$  ka at the scale of the North Island of New Zealand (Litchfield & Berryman, 2005) but is not well constrained. Here, among the four BS-MAM ages from T1 deposits, three are a bit younger ( $11.6 \pm 1.5$  ka to  $14.7 \pm 1.0$  ka; Table 3) and agree with the IRSL multigrain ages of  $13.2 \pm 0.9$  ka and  $11.3 \pm 0.8$  ka of deposits on top of T1 terrace along the Tukituki and Ngaruroro rivers obtained by Litchfield and Rieser (2005). We conclude that T1 aggradation probably ended more recently than the age of  $\sim 15$  ka usually considered, although we cannot exclude a slight age underestimation of our BS-MAM ages due to anomalous fading.

### 5.1.2 | Initial rapid post-T1 incision and knickpoint retreat

The youngest BS-MAM ages of T1 deposits ( $11.6 \pm 1.5$  ka) and the BS-MAM ages of the three highest post-T1 ( $10.1 \pm 0.8$  ka,  $9.2 \pm 0.7$  ka and  $7.7 \pm 1.0$  ka) suggest that the transition between T1 aggradation and incision occurs  $\sim 10$ – $11$  ka. This age estimate agrees with a similar transition from aggradation to incision documented in the North Island of New Zealand on the Waihuka River between 10 and 8 ka (Berryman et al., 2010). Both for Waihuka and Rangitikei, knickpoint propagation followed by a slower rate of downcutting has been proposed as a cause for this transition (Berryman et al., 2010; Bonnet et al., 2019). Our new post-T1 dataset (Figure 7) corroborates this interpretation, although our dataset is too small to investigate along-stream diachronicity of incision initiation as observed in laboratory experiments (Baynes et al., 2020). Nevertheless, several lines of evidence support such evolution. Firstly, major knickpoints with heights of several tens of metres exist along many tributaries of the RR (Figure 11). Secondly, there is a major knickpoint on the RR longitudinal profile, currently located on a major lithological boundary between Plio-Pleistocene deposits of the Wanganui basin and the greywacke basement (Figures 1 and 3). Along-stream distribution of T1 terrace remnants shows that the T1 longitudinal profile merges with the upstream segment that this knickpoint is delimitating (Figure 3). It suggests that this knickpoint is the remnant of the knickpoint or knickzone that propagated along the RR and stopped on this major lithological transition. Thirdly, our data from near Ohingaiti (Figure 1), 104–112 km from the river mouth, allow us to document a very fast local incision, of  $11$ – $15$  mm  $\text{yr}^{-1}$  (see Figure 12), about four to five times higher than the rate we documented using post-T1 terraces data below (Figure 7). We estimate that the propagation of the knickpoint passed Ohingaiti between  $7.7 \pm 1.0$  ka and  $6.9 \pm 1.1$  ka (Figure 12) and has migrated to its current location (Figure 13). Considering 64 km of migration since  $6.9 \pm 1.1$  ka to  $7.7 \pm 1.0$  ka gives an estimate of the knickpoint migration rate of  $8.4 \pm 0.5$  m  $\text{yr}^{-1}$  to  $9.3 \pm 1.8$  m  $\text{yr}^{-1}$ . This estimate is a minimum since knickpoint migration may have stopped at its current location on the lithological transition for an unknown time. This is also a mean value since we consider a linear rate without any dependency on drainage area. The drainage area decreased from 2390 km<sup>2</sup> near Ohingaiti to 710 km<sup>2</sup> at the present knickpoint location (Figure 9E). According to stream power celerity models (Berlin & Anderson, 2007; Crosby & Whipple, 2006), the knickpoint has probably decelerated through time proportionally to this reduction of drainage area, especially at the junction of the major tributaries, between 125 and 150 km (Figures 9E and F).

### 5.1.3 | Decreasing post-T1 incision rate and canyon widening

Following the period of fast incision and knickpoint retreat, the 17 terrace ages below +35/+40 m depict a coherent trend of decreasing age with relative elevation and indicate a reduction of post-T1 incision rate (average  $\sim 3.2$  mm  $\text{yr}^{-1}$ ; Figure 7). No clear longitudinal trend in terrace ages was observed, to infer knickpoint retreat (Baynes et al., 2018). Thus, despite a quite large dispersion of data points, we will consider in the following that, to first-order, incision was quite

uniform and contemporaneous all along the investigated area in this second phase of post-T1 incision (Figure 13).

The post-T1 terraces of the RR are not evenly distributed altitudinally, with a lack in the elevation range where we document a fast incision. Most post-T1 terraces are found below +35/40 m, with a further increase in terrace area below +20 m (see Bonnet et al., 2019 for an extensive study on the altitudinal distribution of terrace threads). Bonnet et al. (2019) proposed that the development of the post-T1 terraces resulted from river migration and enhanced lateral erosion as the incision rate decreased, which was inhibited during the preceding period of fast incision and knickpoint retreat (Hancock & Anderson, 2002).

The cumulative area of post-T1 terraces along-stream increases downstream after the confluence with the three main tributaries and particularly downstream of the confluence with KR (Figure 9D). It is worth noting that the modern width of the RR canyon entrenched in terrace T1 increases in the same way (Figure 9C). It typically is a few hundred metres wide upstream of the RR–KR confluence, and then gradually widens downstream to reach >1500 m near the outlet. We note that the drainage area of RR more than doubles through the confluences with its three main tributaries in only 20 km (Figure 9E). The coincidence between the widening of the RR canyon (Figure 9C), occurrence of post-T1 terraces (Figure 9D) and location of the confluences suggests that the increase in water and sediment flux is an important factor controlling river width and lateral channel migration downstream (Baynes et al., 2020; Bufe et al., 2016, 2019). In the specific case of the Rangitikei drainage network, Baynes et al. (2020) demonstrated that the width of RR and tributaries not only increases with discharge following common hydraulic relationships, but is also set by the area of greywacke basement rocks in the headwaters (Figure 1), which are the main source of bedload material. They propose that it is due to a cover effect (Sklar & Dietrich, 2001), with the high availability of greywacke material protecting the bed of rivers from erosion, driving an increased lateral erosion and widening (Hartshorn, 2002). Among tributaries of the RR, the KR is the river where this effect is the most pronounced (Baynes et al., 2020).

SG-pIRIR  $D_e$  distributions of modern deposits show contrasted trends upstream and downstream of the junction between the RR and the KR (Figures 9A and B). We observe a maximum BS-MAM palaeodose of the RR sediments immediately downstream of the junction of the KR. By considering that the palaeodose measured downstream is the result of mixing between the KR and RR sediments, a simple mass balance indicates that the KR contributes  $\sim 70\%$  of the palaeodose downstream of the RR–KR confluence (see online Supplementary Material). This suggests that the KR has a major influence on the total sediment load, as evidenced by the occurrence of a large alluvial fan in the RR at its junction with the KR (Figure 2D). This is also consistent with recent turbidity measurements (Horizons Regional Council, 2020; Supplementary Table S2), the annual turbidity of the RR being four times higher downstream of its confluence with the KR, and even 23 times higher during floods (Supplementary Table S2).

We suspect from all this evidence that by increasing significantly the flux of coarse-bedload material, the connection of the KR on the RR plays a major role in the widening of the RR canyon observed downstream, as well as the lateral mobility of the RR as testified by

the development of post-T1 terraces. Hence, we propose that after the first phase of post-T1 incision driven by fast retreat of a major knickpoint, incision continued at a slower rate of about  $3 \text{ mm yr}^{-1}$ , with a widening of the canyon downstream of the connection between the KR and the RR related to enhanced lateral mobility of the river, leading to abandonment of many post-T1 terraces. Widening is likely due to the high flux of sediment from the KR, especially of bedload material, which must have resulted in increased erosion and lateral mobility of the RR during its late phase of incision.

## 5.2 | Imprint of geomorphic processes and river dynamics on the equivalent dose distributions of fluvial deposits

### 5.2.1 | Origin of saturated grains

Saturated grains may be derived from bedrock or from fluvial terrace deposits old enough to accumulate trapped charges that would be classified as 'saturated'. Considering the mean  $2 \cdot D_0$  threshold of 300 Gy used here and a mean dose rate of  $3.5 \text{ Gy ka}^{-1}$  (Table 3), grains should be remobilized from former terrace deposits older than 85 ka to give a saturated signal. In our study reach, such old terraces have not been encountered, T1 and T2 being too young. Older terrace remnants are very sparse in our study area, and where present they are attributed to T3, with ages between 50 and 80 ka (Litchfield & Berryman, 2005), still below our saturation threshold. Hence, we conclude that the vast majority, if not all, of the saturated grains have entered the fluvial deposits directly from bedrock erosion, without being significantly light exposed before their burial in the fluvial deposits.

Our luminescence measurements on two bedrock samples from valley flanks bordering the RR canyon (Supplementary Table S3) show a large proportion of saturated grains (74 and 89%), testifying that we are able to correctly identify the vast majority of these grains. The cliffs bordering the Rangitikei canyon are subject to frequent landsliding (Lague et al., 2013; Rees et al., 2020), a likely mechanism for input of saturated grains to the RR without sunlight exposure and bleaching. We conclude that the vast majority of saturated grains identified in terraces and modern deposits are bedrock grains coming from the cliffs bordering the RR canyon, likely through landsliding. It is worth noting that some saturated grains can also come directly from the incision of the channel into underlying bedrock, or from abrasion of cobbles in the channel. These amounts cannot be estimated at present, but we assume that they should be small compared to the volume of sediment entering the system through landslides.

### 5.2.2 | T1 terrace deposits

Equivalent dose distributions for T1 samples show relatively low percentages of saturated grains (7 to 21%; Figure 10B, Table 3) compared to post-T1 terraces (11 to 67%) and modern deposits (6 to 47%). Two mechanisms may account for this observation. First, it could be the direct result of a low influx of saturated bedrock grains to the river, despite the likely high sediment supply that characterized the area at

that time. Alternatively, it could be due to the bleaching effectiveness of the river.

An enhanced sediment flux during T1 formation is inferred from the characteristics of the terrace, which is significantly wider than the modern valley floor and shows evidence of aggradation and braiding (Bonnet et al., 2019; Milne, 1973; Pillans et al., 1993), these characteristics being commonly related to climatically induced periods of enhanced erosion rate at the catchment scale (Fuller et al., 2009; Hancock & Anderson, 2002; Schanz et al., 2018). Moreover, an increase in hillslope erosion contemporary to deposition of T1 alluvium is evidenced in the North Island of New Zealand by erosion of tephra of known age that mantled the topography, likely by mass movements on hillslopes (solifluction) under periglacial colder and drier climatic conditions, and reduced vegetation cover (see synthesis in Clement & Fuller, 2007 and Litchfield & Berryman, 2005). If the grains in the T1 terrace deposits are indeed sourced from hillslopes, this may explain the low percentage of saturated grains. On hillslopes, subaerial resetting of the luminescence signal occurs at the surface, but due to bioturbation processes grains in the upper tens of centimetres are also likely to be exposed to sunlight (Reimann et al., 2017). Therefore, a low level of saturated grains within the supplied material is not incompatible with a late Pleistocene enhanced erosion on hillslopes by mass wasting, as long as the mobilized material consists of soils instead of unweathered (i.e. saturated) bedrock. Bleaching during transport by solifluction is also a possibility, however the efficiency of bleaching in this context is relatively unknown.

The low level of saturation of T1 deposits could alternatively result from an efficient bleaching of the signal by sunlight exposure during fluvial transport. Longitudinal bleaching was potentially enhanced for T1 because of the particular braided pattern of the RR at that time, which allows cumulative bleaching opportunities during successive transport events (McGuire & Rhodes, 2015a; Stokes et al., 2001). The development of such fluvial systems requires high sediment supply (Mueller & Pitlick, 2014), as already pointed out above, and they are also characterized by short transport length of the sediments during a single flood (Davy & Lague, 2009; Kasprak et al., 2015), coupled to high lateral mobility and very dynamic planform of channels and bars. We propose that the specific characteristics of braided systems, in particular short transport distances during flood events and high lateral mobility, favour grain exposure to sunlight and participate in the observed low saturation level of T1 deposits. As we cannot discriminate whether low saturation level in T1 results from supply, along-stream transport or a combination of the two, we suggest that this topic deserves attention in future work.

### 5.2.3 | Post-T1 terraces

Among post-T1 terraces, those at relative elevations of +40 to +20 m show the highest percentage of saturated grains (Figure 10B) and longitudinal trends of saturation increasing downstream (Figures 8A and B). Having such high saturation rates in river sediments, which can exceed 50%, necessarily implies high inputs of saturated grains, above the bleaching capacity by river transport. According to our geomorphic model for the Holocene evolution of RR, terraces in this elevation range were the first to be formed after the retreat of a major knickpoint during the initial stage of post-T1

incision. We propose that after the passage of this knickpoint, the RR canyon was narrow, possibly as upstream of the RR–KR connection today (Figure 2C), with very few post-T1 terraces, and that major canyon flank slides were responsible for a very large incorporation of saturated grains directly from the bedrock into the RR sediments (Figure 6, process 2), now forming post-T1 terraces between +40 and +20 m.

The gradual longitudinal increase of saturation in both the subgroups of terraces gathered by relative elevation of 40–30 m (Figure 8A) and 30–20 m (Figure 8B) indicates that it is not a localized feature, related for instance to a single landslide or to the junction of a tributary. Actually, the saturation of fluvial sediments downstream a local release of a stock of saturated grains could only decrease downward, either by a dilution effect or by bleaching, so that the longitudinal increase in saturation necessarily implies continuous inputs all along the river. This also implies an input rate higher than the bleaching rate (process 2 dominates over process 1 in Figure 6).

As discussed previously, two post-T1 samples from the elevation range +30 to +40 m (RO\_13 at +38 m and RO\_17 at +31 m; Figure 7) gave BS-MAM apparent ages that appear too old for their geomorphic position. According to our interpretation, these terraces formed in the context of high input of bedrock grains through landsliding following knickpoint retreat, and likely of high sediment flux from valley flanks. Accordingly, the characteristics of  $D_e$  distribution of these samples indicate that their grains have been very poorly bleached: they are characterized by a high proportion of saturated grains (46 and 40%), low proportion of well-bleached ones (11 and 13%) and high inherited doses (116 and 107 Gy); Table 3. We suggest that their age overestimation using the BS-MAM protocol may imply that these deposits contained no bleached grains at the time of deposition (i.e. the assumption underlying the use of BS-MAM that part of the population is well bleached is not met for these samples).

For post-T1 terraces below +40 m, the percentage of saturated grains gradually decreases with elevation (Figure 10B), while the percentage of incompletely bleached grains and/or grains with an inherited dose increases, and the percentage of well-bleached grains remains constant (Figures 8). We propose that two mechanisms may account for the decreasing trend in saturation: a lower input of saturated grains from bedrock, or better bleaching conditions during fluvial transport. This second mechanism would likely have resulted in a larger proportion of well-bleached grains, which is not observed here (Figures 8D and E). This leads us to favour the first hypothesis, which is also consistent with the geomorphic context.

We propose that the decrease in influx of saturated bedrock grains to the river is mainly due to the reduction of contact area between the RR and the bordering cliffs as the post-T1 terraces developed on river sides. In fact, once a terrace is abandoned (see e.g. Figure 4B and the sketch in Figure 8F), the river is no longer in contact with its bordering cliff. The analysis of Bonnet et al. (2019) showed that most of the post-T1 terraces are found between +20 m and the present river floor (see their figure 2) and they interpret this occurrence as the result of an increased lateral migration of the RR during the latter incision. We then propose that the progressive decreasing trend in saturation from post-T1 terraces at +30/40 m reflects a decrease in the contact area between the river and the canyon flanks as the post-T1 terraces are abandoned on river sides.

Upstream of the KR junction, where the RR has a canyon shape with very few post-T1 terraces (Figures 2C and 4A), the percentage of direct contact of the river with the bedrock on canyon flanks is 85% (from 124 to 164 km from river mouth). Downstream of the junction, where the canyon widens (Figure 10C) and most post-T1 terraces are observed (Figure 9D), it drops to 33% on the right side of the RR and 50% on its left side (from 124 to 60 km from river mouth). Then, we propose that the progressive decrease in saturation of post-T1 terraces with elevation is rather the sign of a reduction in landslides of canyon flanks.

## 6 | CONCLUSIONS

This study evaluates the use of a single-grain pIRIR signal of feldspars from fluvial deposits for retrieving information on sediment sources and pathways. We focus our analysis on terraces and modern deposits of the Rangitikei River and its main tributary, Kawhatau (New Zealand).

Using the BS-MAM of Cunningham and Wallinga (2012), we provide the first absolute age of a main terrace T2 ( $32.1 \pm 3.9$  ka) and constrain the age for terrace T1 to  $11.6 \pm 1.5$  ka to  $17.4 \pm 1.9$  ka. In addition, we show that abandonment of terrace T1 occurred at  $\sim 11$  ka and was followed by a first period of fast incision, likely through knickpoint propagation. Locally, in the upper part of the RR, we dated the passage of this knickpoint between  $7.7 \pm 1.0$  ka and  $6.9 \pm 1.1$  ka and estimate that it has subsequently retreated at a mean rate of  $8.4 \pm 0.5$  m  $\text{yr}^{-1}$  to  $9.3 \pm 1.8$  m  $\text{yr}^{-1}$ .

After this period of rapid incision, incision slowed down to a mean rate of  $\sim 3.2$  mm  $\text{yr}^{-1}$ . We document a longitudinal change in incision dynamics of the river between its upstream and downstream parts, the transition occurring at the junction of the KR with the RR. Upstream of this confluence, the RR forms a narrow and deep canyon, while downstream it forms numerous cut terraces (post-T1) in a valley that gradually widens. We attributed this change to a high influx of sediment from the KR, which promotes lateral erosion and mobility of the Rangitikei downstream.

We propose that the percentage of grains with saturated pIRIR signals reflects direct bedrock input to the river sediments, mostly through landsliding of canyon flanks during incision. The percentage of saturated grains is very low in the braided T1 terrace, while strikingly high percentages are found for terrace deposits formed shortly after the passage of the knickpoint. The percentage of saturated grains decreased when incision slowed down and the canyon widened. All these trends can be explained by increases and reduction in the contact area between the river and its flanks, affecting the likelihood of landslides. The percentage of well-bleached grains reflects opportunities for bleaching in the river or prior to entering the river. The highest percentages were observed for the braided fluvial system of T1.

Our study documents a large spatio-temporal variability of SG-pIRIR  $D_e$  distributions in fluvial deposits. This variability reflects a change in the source and pathways of sediment grains and can be linked to the geomorphological development of the RR. Thereby, our study confirms the great potential of SG-pIRIR for investigating erosion and transport processes in fluvial systems in the past and present.



## ACKNOWLEDGEMENTS

This work was funded by the Franco-Dutch Hubert Curien Partnership (Van Gogh Programme No. VGP.19/00012) and CNRS-INSU TelluS-SYSTER Programme (to S. Bonnet).

## DATA AVAILABILITY STATEMENT

All data are available on request from the corresponding author.

## ORCID

Anne Guyez  <https://orcid.org/0000-0003-3246-8700>

## REFERENCES

- Ahnert, F. (1970) Functional relationships between denudation, relief, and uplift in large, mid-latitude drainage basins. *American Journal of Science*, 268(3), 243–263. Available from: <https://doi.org/10.2475/ajs.268.3.243>
- Aitken, M.J. (1998) *Introduction to Optical Dating: The Dating of Quaternary Sediments by the Use of Photon-Stimulated Luminescence*. Oxford: Clarendon Press.
- Anon. (2020) Horizons Regional Council [online]. Available at <https://envirodata.horizons.govt.nz/>
- Baynes, E.R.C., Lague, D., Attal, M., Gangloff, A., Kirstein, L.A. & Dugmore, A.J. (2018) River self-organisation inhibits discharge control on waterfall migration. *Scientific Reports*, 8(1), 2444. <https://doi.org/10.1038/s41598-018-20767-6>
- Baynes, E.R.C., Lague, D., Steer, P., Bonnet, S. & Illien, L. (2020) Sediment flux-driven channel geometry adjustment of bedrock and mixed gravel-bedrock rivers. *Earth Surface Processes and Landforms*, 45(14), 3714–3731. Available from: <https://doi.org/10.1002/esp.4996>
- Berger, G.W. (1990) Effectiveness of natural zeroing of the thermoluminescence in sediments. *Journal of Geophysical Research*, 95(B8), 12375. Available from: <https://doi.org/10.1029/JB095iB08p12375>
- Berlin, M.M. & Anderson, R.S. (2007) Modeling of knickpoint retreat on the Roan Plateau, western Colorado. *Journal of Geophysical Research*, 112(F3), F03S06. Available from: <https://doi.org/10.1029/2006JF000553>
- Berryman, K., Marden, M., Palmer, A., Wilson, K., Mazengarb, C. & Litchfield, N. (2010) The post-glacial downcutting history in the Waihuka tributary of Waipaoa River, Gisborne district: Implications for tectonics and landscape evolution in the Hikurangi subduction margin, New Zealand. *Marine Geology*, 270(1–4), 55–71. Available from: <https://doi.org/10.1016/j.margeo.2009.10.001>
- Binnie, S.A., Phillips, W.M., Summerfield, M.A., Fifield, L.K. & Spotila, J.A. (2010) Tectonic and climatic controls of denudation rates in active orogens: The San Bernardino Mountains, California. *Geomorphology*, 118(3–4), 249–261. Available from: <https://doi.org/10.1016/j.geomorph.2010.01.005>
- Biswas, R.H., Herman, F., King, G.E. & Braun, J. (2018) Thermoluminescence of feldspar as a multi-thermochronometer to constrain the temporal variation of rock exhumation in the recent past. *Earth and Planetary Science Letters*, 495, 56–68. Available from: <https://doi.org/10.1016/j.epsl.2018.04.030>
- Blair, M.W., Yuhikara, E.G. & McKeever, S.W.S. (2005) Experiences with single-aliquot OSL procedures using coarse-grain feldspars. *Radiation Measurements*, 39(4), 361–374. Available from: <https://doi.org/10.1016/j.radmeas.2004.05.008>
- Bonnet, S., Reimann, T., Wallinga, J., Lague, D., Davy, P. & Lacoste, A. (2019) Landscape dynamics revealed by luminescence signals of feldspars from fluvial terraces. *Scientific Reports*, 9(1), 8569. <https://doi.org/10.1038/s41598-019-44533-4>
- Brown, E.T., Stallard, R.F., Larsen, M.C., Raisbeck, G.M. & Yiou, F. (1995) Denudation rates determined from the accumulation of in situ-produced  $^{10}\text{Be}$  in the Luquillo Experimental Forest, Puerto Rico. *Earth and Planetary Science Letters*, 129(1–4), 193–202. Available from: [https://doi.org/10.1016/0012-821X\(94\)00249-X](https://doi.org/10.1016/0012-821X(94)00249-X)
- Brown, N.D. (2020) Which geomorphic processes can be informed by luminescence measurements? *Geomorphology*, 367, 107296. Available from: <https://doi.org/10.1016/j.geomorph.2020.107296>
- Bufe, A., Paola, C. & Burbank, D.W. (2016) Fluvial beveling of topography controlled by lateral channel mobility and uplift rate. *Nature Geoscience*, 9(9), 706–710. Available from: <https://doi.org/10.1038/ngeo2773>
- Bufe, A., Turowski, J.M., Burbank, D.W., Paola, C., Wickert, A.D. & Tofelde, S. (2019) Controls on the lateral channel-migration rate of braided channel systems in coarse non-cohesive sediment. *Earth Surface Processes and Landforms*, 44(14), 2823–2836. Available from: <https://doi.org/10.1002/esp.4710>
- Carretier, S., Regard, V., Vassallo, R., Aguilar, G., Martinod, J., Riquelme, R., Pepin, E., Charrier, R., Hérail, G., Fariás, M., Guyot, J.L., Vargas, G. & Lagane, C. (2013) Slope and climate variability control of erosion in the Andes of Central Chile. *Geology*, 41(2), 195–198. Available from: <https://doi.org/10.1130/G33735.1>
- Chamberlain, E.L. & Wallinga, J. (2019) Seeking enlightenment of fluvial sediment pathways by optically stimulated luminescence signal bleaching of river sediments and deltaic deposits. *Earth Surface Dynamics*, 7(3), 723–736. Available from: <https://doi.org/10.5194/esurf-7-723-2019>
- Chamberlain, E.L., Wallinga, J. & Shen, Z. (2018) Luminescence age modeling of variably-bleached sediment: Model selection and input. *Radiation Measurements*, 120, 221–227. Available from: <https://doi.org/10.1016/j.radmeas.2018.06.007>
- Chen, S.-A., Michaelides, K., Singer, M.B. & Richards, D.A. (2021) Global analysis of short- versus long-term drainage basin erosion rates. *Earth Surface Dynamics Discussions*. Available from: <https://doi.org/10.5194/esurf-2021-7>
- Clement, A.J.H. & Fuller, I.C. (2007) Fluvial responses to environmental change in the North Island, New Zealand, during the past c. 30 ka recorded in river terrace sequences: A review and model for river behaviour. *New Zealand Journal of Geology and Geophysics*, 50(2), 101–116. Available from: <https://doi.org/10.1080/00288300709509824>
- Clift, P.D., Blusztajn, J. & Nguyen, A.D. (2006) Large-scale drainage capture and surface uplift in eastern Tibet–SW China before 24 Ma inferred from sediments of the Hanoi Basin, Vietnam. *Geophysical Research Letters*, 33(19), L19403. Available from: <https://doi.org/10.1029/2006GL027772>
- Covault, J.A., Craddock, W.H., Romans, B.W., Fildani, A. & Gosai, M. (2013) Spatial and temporal variations in landscape evolution: Historic and longer-term sediment flux through global catchments. *The Journal of Geology*, 121(1), 35–56. Available from: <https://doi.org/10.1086/668680>
- Crosby, B.T. & Whipple, K.X. (2006) Knickpoint initiation and distribution within fluvial networks: 236 waterfalls in the Waipaoa River, North Island, New Zealand. *Geomorphology*, 82(1–2), 16–38. Available from: <https://doi.org/10.1016/j.geomorph.2005.08.023>
- Cunningham, A.C. & Wallinga, J. (2012) Realizing the potential of fluvial archives using robust OSL chronologies. *Quaternary Geochronology*, 12, 98–106. Available from: <https://doi.org/10.1016/j.quageo.2012.05.007>
- Davies-Colley, R.J. & Nagels, J.W. (2008) Predicting light penetration into river waters. *Journal of Geophysical Research*, 113(G3), G03028. Available from: <https://doi.org/10.1029/2008JG000722>
- Davy, P. & Lague, D. (2009) Fluvial erosion/transport equation of landscape evolution models revisited. *Journal of Geophysical Research*, 114(F3), F03007. Available from: <https://doi.org/10.1029/2008JF001146>
- Ditlefsen, C. (1992) Bleaching of K-feldspars in turbid water suspensions: A comparison of photo- and thermoluminescence signals. *Quaternary Science Reviews*, 11(1–2), 33–38. Available from: [https://doi.org/10.1016/0277-3791\(92\)90039-B](https://doi.org/10.1016/0277-3791(92)90039-B)
- Fuller, I.C., Large, A.R.G., Charlton, M.E., Heritage, G.L. & Milan, D.J. (2003) Reach-scale sediment transfers: An evaluation of two morphological budgeting approaches. *Earth Surface Processes and Landforms*, 28(8), 889–903. Available from: <https://doi.org/10.1002/esp.1011>

- Fuller, T.K., Perg, L.A., Willenbring, J.K. & Lepper, K. (2009) Field evidence for climate-driven changes in sediment supply leading to strath terrace formation. *Geology*, 37(5), 467–470. Available from: <https://doi.org/10.1130/G25487A.1>
- Furbish, D.J., Roering, J.J., Keen-Zebert, A., Almond, P., Doane, T.H. & Schumer, R. (2018) Soil particle transport and mixing near a hillslope crest: 2. Cosmogenic nuclide and optically stimulated luminescence tracers. *Journal of Geophysical Research: Earth Surface*, 123(5), 1078–1093. Available from: <https://doi.org/10.1029/2017JF004316>
- Galbraith, R.F., Roberts, R.G., Laslett, G.M., Yoshida, H. & Olley, J.M. (1999) Optical dating of single and multiple grains of quartz from Jinmium rock shelter, northern Australia: Part I, experimental design and statistical models. *Archaeometry*, 41(2), 339–364. Available from: <https://doi.org/10.1111/j.1475-4754.1999.tb00987.x>
- Galy, A. & France-Lanord, C. (2001) Higher erosion rates in the Himalaya: Geochemical constraints on riverine fluxes. *Geology*, 29(1), 23–26. Available from: [https://doi.org/10.1130/0091-7613\(2001\)029<0023:HERITH>2.0.CO;2](https://doi.org/10.1130/0091-7613(2001)029<0023:HERITH>2.0.CO;2)
- Garzanti, E., Vezzoli, G., Andò, S., Lavé, J., Attal, M., France-Lanord, C. & DeCelles, P. (2007) Quantifying sand provenance and erosion (Marsyandi River, Nepal Himalaya). *Earth and Planetary Science Letters*, 258(3–4), 500–515. Available from: <https://doi.org/10.1016/j.epsl.2007.04.010>
- Glignani, L.A., Cohen, T.J., Meyer, M. & Molenaar, A. (2017) Variations in luminescence properties of quartz and feldspar from modern fluvial sediments in three rivers. *Quaternary Geochronology*, 41, 70–82. Available from: <https://doi.org/10.1016/j.quageo.2017.06.005>
- Godard, V., Bourles, D.L., Spinabell, F., Burbank, D.W., Bookhagen, B., Fisher, G.B., Moulin, A. & Leanni, L. (2014) Dominance of tectonics over climate in Himalayan denudation. *Geology*, 42(3), 243–246. Available from: <https://doi.org/10.1130/G35342.1>
- Godfrey-Smith, D.I., Huntley, D.J. & Chen, W.-H. (1988) Optical dating studies of quartz and feldspar sediment extracts. *Quaternary Science Reviews*, 7(3–4), 373–380. Available from: [https://doi.org/10.1016/0277-3791\(88\)90032-7](https://doi.org/10.1016/0277-3791(88)90032-7)
- Granger, D.E., Kirchner, J.W. & Finkel, R. (1996) Spatially averaged long-term erosion rates measured from in situ-produced cosmogenic nuclides in alluvial sediment. *The Journal of Geology*, 104(3), 249–257. Available from: <https://doi.org/10.1086/629823>
- Gray, H.J., Jain, M., Sawakuchi, A.O., Mahan, S.A. & Tucker, G.E. (2019) Luminescence as a sediment tracer and provenance tool. *Reviews of Geophysics*, 57(3), 987–1017. Available from: <https://doi.org/10.1029/2019RG000646>
- Gray, H.J., Keen-Zebert, A., Furbish, D.J., Tucker, G.E. & Mahan, S.A. (2020) Depth-dependent soil mixing persists across climate zones. *Proceedings of the National Academy of Sciences*, 117(16), 8750–8756. Available from: <https://doi.org/10.1073/pnas.1914140117>
- Gray, H.J. & Mahan, S.A. (2015) Variables and potential models for the bleaching of luminescence signals in fluvial environments. *Quaternary International*, 362, 42–49. Available from: <https://doi.org/10.1016/j.quaint.2014.11.007>
- Gray, H.J., Tucker, G.E. & Mahan, S.A. (2018) Application of a luminescence-based sediment transport model. *Geophysical Research Letters*, 45, 6071–6080. Available from: <https://doi.org/10.1029/2018GL078210>
- Gray, H.J., Tucker, G.E., Mahan, S.A., McGuire, C. & Rhodes, E.J. (2017) On extracting sediment transport information from measurements of luminescence in river sediment. *Journal of Geophysical Research: Earth Surface*, 122(3), 654–677. Available from: <https://doi.org/10.1002/2016JF003858>
- Guerit, L., Barrier, L., Jolivet, M., Fu, B. & Métivier, F. (2016) Denudation intensity and control in the Chinese Tian Shan: New constraints from mass balance on catchment–alluvial fan systems. *Earth Surface Processes and Landforms*, 41(8), 1088–1106. Available from: <https://doi.org/10.1002/esp.3890>
- Guralnik, B., Ankjærgaard, C., Jain, M., Murray, A.S., Müller, A., Wälle, M., Lowick, S.E., Preusser, F., Rhodes, E.J., Wu, T.S., Mathew, G. & Herman, F. (2015) OSL-thermochronometry using bedrock quartz: A note of caution. *Quaternary Geochronology*, 25, 37–48. Available from: <https://doi.org/10.1016/j.quageo.2014.09.001>
- Guralnik, B., Jain, M., Herman, F., Paris, R.B., Harrison, T.M., Murray, A.S., Valla, P.G. & Rhodes, E.J. (2013) Effective closure temperature in leaky and/or saturating thermochronometers. *Earth and Planetary Science Letters*, 384, 209–218. Available from: <https://doi.org/10.1016/j.epsl.2013.10.003>
- Haddadchi, A., Olley, J. & Pietsch, T. (2016) Using LM-OSL of quartz to distinguish sediments derived from surface-soil and channel erosion. *Hydrological Processes*, 30, 637–647. Available from: <https://doi.org/10.1002/hyp.10646>
- Hancock, G.S. & Anderson, R.S. (2002) Numerical modeling of fluvial strath-terrace formation in response to oscillating climate. *Geological Society of America Bulletin*, 114(9), 1131–1142. Available from: [https://doi.org/10.1130/0016-7606\(2002\)114<1131:NMOFST>2.0.CO;2](https://doi.org/10.1130/0016-7606(2002)114<1131:NMOFST>2.0.CO;2)
- Hartshorn, K. (2002) Climate-driven bedrock incision in an active mountain belt. *Science*, 297(5589), 2036–2038. Available from: <https://doi.org/10.1126/science.1075078>
- Herman, F., Rhodes, E.J., Braun, J. & Heiniger, L. (2010) Uniform erosion rates and relief amplitude during glacial cycles in the Southern Alps of New Zealand, as revealed from OSL-thermochronology. *Earth and Planetary Science Letters*, 297(1–2), 183–189. Available from: <https://doi.org/10.1016/j.epsl.2010.06.019>
- Hinderer, M., Pflanz, D. & Schneider, S. (2013) Chemical denudation rates in the humid tropics of East Africa and comparison with <sup>10</sup>Be-derived erosion rates. *Procedia Earth and Planetary Science*, 7, 360–364. Available from: <https://doi.org/10.1016/j.proeps.2013.03.047>
- Huntley, D.J., Godfrey-Smith, D.I. & Thewalt, M.L. (1985) Optical dating of sediments. *Nature*, 313(5998), 105–107. Available from: <https://doi.org/10.1038/313105a0>
- Jain, M., Murray, A.S. & Botter-Jensen, L. (2004) Optically stimulated luminescence dating: How significant is incomplete light exposure in fluvial environments? *Quaternaire*, 15(1), 143–157. Available from: <https://doi.org/10.3406/quate.2004.1762>
- Journeaux, T.D., Kamp, P.J. & Naish, T. (1996) Middle Pliocene cyclothem, Mangaweka region, Wanganui Basin, New Zealand: A lithostratigraphic framework. *New Zealand Journal of Geology and Geophysics*, 39(1), 135–149. Available from: <https://doi.org/10.1080/00288306.1996.9514700>
- Kamp, P.J.J., Journeaux, T.D. & Morgans, H.E.G. (1998) Cyclostratigraphy of middle Pliocene mid shelf to upper slope strata, eastern Wanganui Basin (New Zealand): Correlations to the deep sea isotope record. *Sedimentary Geology*, 117(3–4), 165–192. Available from: [https://doi.org/10.1016/S0037-0738\(98\)00016-5](https://doi.org/10.1016/S0037-0738(98)00016-5)
- Kasprak, A., Wheaton, J.M., Ashmore, P.E., Hensleigh, J.W. & Peirce, S. (2015) The relationship between particle travel distance and channel morphology: Results from physical models of braided rivers. *Journal of Geophysical Research: Earth Surface*, 120(1), 55–74. Available from: <https://doi.org/10.1002/2014JF003310>
- Kemp, D.B., Sadler, P.M. & Vanacker, V. (2020) The human impact on North American erosion, sediment transfer, and storage in a geologic context. *Nature Communications*, 11(1), 6012. <https://doi.org/10.1038/s41467-020-19744-3>
- King, G.E., Guralnik, B., Valla, P.G. & Herman, F. (2016) Trapped-charge thermochronometry and thermometry: A status review. *Chemical Geology*, 446, 3–17. Available from: <https://doi.org/10.1016/j.chemgeo.2016.08.023>
- Kirchner, J.W., Finkel, R.C., Riebe, C.S., Granger, D.E., Clayton, J.L., King, J.G. & Megahan, W.F. (2001) Mountain erosion over 10 yr, 10 ky, and 10 my time scales. *Geology*, 29(7), 591–594. Available from: [https://doi.org/10.1130/0091-7613\(2001\)029<0591:MEOKY>2.0.CO;2](https://doi.org/10.1130/0091-7613(2001)029<0591:MEOKY>2.0.CO;2)
- Kreutzer, S., Schmidt, C., Fuchs, M.C., Dietze, M., Fischer, M. & Fuchs, M. (2012) Introducing an R package for luminescence dating analysis. *Ancient TL*, 30, 1–8.
- Kristensen, J.A., Thomsen, K.J., Murray, A.S., Buylaert, J.-P., Jain, M. & Breuning-Madsen, H. (2015) Quantification of termite bioturbation in a savannah ecosystem: Application of OSL dating. *Quaternary Geochronology*, 30, 334–341. Available from: <https://doi.org/10.1016/j.quageo.2015.02.026>

- Kuhlemann, J., Frisch, W., Dunkl, I., Székely, B. & Spiegel, C. (2001) Miocene shifts of the drainage divide in the Alps and their foreland basin. *Zeitschrift für Geomorphologie*, 45(2), 239–265. Available from: <https://doi.org/10.1127/zfg/45/2001/239>
- Lague, D., Brodu, N. & Leroux, J. (2013) Accurate 3D comparison of complex topography with terrestrial laser scanner: Application to the Rangitikei canyon (N-Z). *ISPRS Journal of Photogrammetry and Remote Sensing*, 82, 10–26. Available from: <https://doi.org/10.1016/j.isprsjprs.2013.04.009>
- Lehmann, B., Valla, P.G., King, G.E. & Herman, F. (2018) Investigation of OSL surface exposure dating to reconstruct post-LIA glacier fluctuations in the French Alps (Mer de Glace, Mont Blanc massif). *Quaternary Geochronology*, 44, 63–74. Available from: <https://doi.org/10.1016/j.quageo.2017.12.002>
- Litchfield, N. & Berryman, K. (2006) Relations between postglacial fluvial incision rates and uplift rates in the North Island, New Zealand. *Journal of Geophysical Research*, 111(F2), F02007. Available from: <https://doi.org/10.1029/2005JF000374>
- Litchfield, N.J. & Berryman, K.R. (2005) Correlation of fluvial terraces within the Hikurangi Margin, New Zealand: Implications for climate and baselevel controls. *Geomorphology*, 68(3–4), 291–313. Available from: <https://doi.org/10.1016/j.geomorph.2004.12.001>
- Litchfield, N.J. & Rieser, U. (2005) Optically stimulated luminescence age constraints for fluvial aggradation terraces and loess in the eastern North Island, New Zealand. *New Zealand Journal of Geology and Geophysics*, 48(4), 581–589. Available from: <https://doi.org/10.1080/00288306.2005.9515135>
- Liu, H., Kishimoto, S., Takagawa, T., Shirai, M. & Sato, S. (2009) Investigation of the sediment movement along the Tenryu–Enshunada fluvial system based on feldspar thermoluminescence properties. *Journal of Coastal Research*, 255, 1096–1105. Available from: <https://doi.org/10.2112/08-1065.1>
- Lupker, M., Blard, P.-H., Lavé, J., France-Lanord, C., Leanni, L., Puchol, N., Charreau, J. & Bourlès, D. (2012) <sup>10</sup>Be-derived Himalayan denudation rates and sediment budgets in the Ganga basin. *Earth and Planetary Science Letters*, 333–334, 146–156. Available from: <https://doi.org/10.1016/j.epsl.2012.04.020>
- McGuire, C. & Rhodes, E.J. (2015a) Determining fluvial sediment virtual velocity on the Mojave River using K-feldspar IRSL: Initial assessment. *Quaternary International*, 362, 124–131. Available from: <https://doi.org/10.1016/j.quaint.2014.07.055>
- McGuire, C. & Rhodes, E.J. (2015b) Downstream MET-IRSL single-grain distributions in the Mojave River, southern California: Testing assumptions of a virtual velocity model. *Quaternary Geochronology*, 30, 239–244. Available from: <https://doi.org/10.1016/j.quageo.2015.02.004>
- Milliman, J.D. & Meade, R.H. (1983) World-wide delivery of river sediment to the oceans. *The Journal of Geology*, 91(1), 1–21. Available from: <https://doi.org/10.1086/628741>
- Milliman, J.D. & Syvitski, J.P.M. (1992) Geomorphic/tectonic control of sediment discharge to the ocean: The importance of small mountainous rivers. *The Journal of Geology*, 100(5), 525–544. Available from: <https://doi.org/10.1086/629606>
- Milne, J.D.G. (1973) *Map and Sections of River Terraces in the Rangitikei Basin, North Island, New Zealand*. New Zealand Soil Survey Report No. 4.
- Mudd, S.M. (2017) Detection of transience in eroding landscapes. *Earth Surface Processes and Landforms*, 42(1), 24–41. Available from: <https://doi.org/10.1002/esp.3923>
- Mueller, E.R. & Pitlick, J. (2014) Sediment supply and channel morphology in mountain river systems: 2. Single thread to braided transitions. *Journal of Geophysical Research: Earth Surface*, 119(7), 1516–1541. Available from: <https://doi.org/10.1002/2013JF003045>
- Murray, A.S. & Roberts, R.G. (1997) Determining the burial time of single grains of quartz using optically stimulated luminescence. *Earth and Planetary Science Letters*, 152(1–4), 163–180. Available from: [https://doi.org/10.1016/S0012-821X\(97\)00150-7](https://doi.org/10.1016/S0012-821X(97)00150-7)
- Murray, A.S., Thomsen, K.J., Masuda, N., Buylaert, J.P. & Jain, M. (2012) Identifying well-bleached quartz using the different bleaching rates of quartz and feldspar luminescence signals. *Radiation Measurements*, 47(9), 688–695. Available from: <https://doi.org/10.1016/j.radmeas.2012.05.006>
- Norton, K.P., von Blanckenburg, F., Schlunegger, F. & Kubik, P.W. (2006). Knickpoint migration in the Swiss Mittelland revealed by basin-averaged cosmogenic nuclide derived erosion rates, (Terra Nostra; 2006/3), GV International Conference 2006 and 96th Annual Meeting of the Geologische Vereinigung e. V. (Potsdam 2006) (Berlin).
- Ouimet, W.B., Whipple, K.X. & Granger, D.E. (2009) Beyond threshold hillslopes: Channel adjustment to base-level fall in tectonically active mountain ranges. *Geology*, 37(7), 579–582. Available from: <https://doi.org/10.1130/G30013A.1>
- Pillans, B. (1990) Pleistocene marine terraces in New Zealand: A review. *New Zealand Journal of Geology and Geophysics*, 33(2), 219–231. Available from: <https://doi.org/10.1080/00288306.1990.10425680>
- Pillans, B. (1991) New Zealand Quaternary stratigraphy: An overview. *Quaternary Science Reviews*, 10(5), 405–418. Available from: [https://doi.org/10.1016/0277-3791\(91\)90004-E](https://doi.org/10.1016/0277-3791(91)90004-E)
- Pillans, B., McGlone, M., Palmer, A., Mildenhall, D., Alloway, B. & Berger, G. (1993) The last glacial maximum in central and southern North Island, New Zealand: A paleoenvironmental reconstruction using the Kawakawa Tephra Formation as a chronostratigraphic marker. *Palaeogeography, Palaeoclimatology, Palaeoecology*, 101(3–4), 283–304. Available from: [https://doi.org/10.1016/0031-0182\(93\)90020-J](https://doi.org/10.1016/0031-0182(93)90020-J)
- Porat, N., Zilberman, E., Amit, R. & Enzel, Y. (2001) Residual ages of modern sediments in an hyperarid region, Israel. *Quaternary Science Reviews*, 20(5–9), 795–798. Available from: [https://doi.org/10.1016/S0277-3791\(00\)00021-4](https://doi.org/10.1016/S0277-3791(00)00021-4)
- Portenga, E.W. & Bierman, P.R. (2011) Understanding Earth's eroding surface with <sup>10</sup>Be. *GSA Today*, 21(8), 4–10. Available from: <https://doi.org/10.1130/G111A.1>
- Pulford, A. & Stern, T. (2004) Pliocene exhumation and landscape evolution of central North Island, New Zealand: The role of the upper mantle. *Journal of Geophysical Research: Earth Surface*, 109, F01016. Available from: <https://doi.org/10.1029/2003JF000046>
- Rees, C., Palmer, A. & Palmer, J. (2020) Litho-structural controls on Quaternary landslide distribution in the Rangitikei hill country, North Island, New Zealand. *New Zealand Journal of Geology and Geophysics*, 63(1), 90–109. Available from: <https://doi.org/10.1080/00288306.2019.1629966>
- Reimann, T., Notenboom, P.D., De Schipper, M.A. & Wallinga, J. (2015) Testing for sufficient signal resetting during sediment transport using a polymineral multiple-signal luminescence approach. *Quaternary Geochronology*, 25, 26–36. Available from: <https://doi.org/10.1016/j.quageo.2014.09.002>
- Reimann, T., Román-Sánchez, A., Vanwalleghe, T. & Wallinga, J. (2017) Getting a grip on soil reworking – single-grain feldspar luminescence as a novel tool to quantify soil reworking rates. *Quaternary Geochronology*, 42, 1–14. Available from: <https://doi.org/10.1016/j.quageo.2017.07.002>
- Reimann, T., Thomsen, K.J., Jain, M., Murray, A.S. & Frechen, M. (2012) Single-grain dating of young sediments using the pIRIR signal from feldspar. *Quaternary Geochronology*, 11, 28–41. Available from: <https://doi.org/10.1016/j.quageo.2012.04.016>
- Rittenour, T.M. (2008) Luminescence dating of fluvial deposits: Applications to geomorphic, palaeoseismic and archaeological research. *Boreas*, 37(4), 613–635. Available from: <https://doi.org/10.1111/j.1502-3885.2008.00056.x>
- Román-Sánchez, A., Laguna, A., Reimann, T., Giráldez, J.V., Peña, A. & Vanwalleghe, T. (2019a) Bioturbation and erosion rates along the soil–hillslope conveyor belt, part 2: Quantification using an analytical solution of the diffusion–advection equation. *Earth Surface Processes and Landforms*, 44(10), 2066–2080. Available from: <https://doi.org/10.1002/esp.4626>
- Román-Sánchez, A., Reimann, T., Wallinga, J. & Vanwalleghe, T. (2019b) Bioturbation and erosion rates along the soil–hillslope conveyor belt, part 1: Insights from single-grain feldspar luminescence. *Earth Surface Processes and Landforms*, 44(10), 2051–2065. Available from: <https://doi.org/10.1002/esp.4628>

- Sawakuchi, A.O., Jain, M., Mineli, T.D., Nogueira, L., Bertassoli, D.J., Jr., Häggi, C., Sawakuchi, H.O., Pupim, F.N., Grohmann, C.H. & Chiessi, C.M. (2018) Luminescence of quartz and feldspar fingerprints provenance and correlates with the source area denudation in the Amazon River basin. *Earth and Planetary Science Letters*, 492, 152–162. Available from: <https://doi.org/10.1016/j.epsl.2018.04.006>
- Schanz, S.A., Montgomery, D.R., Collins, B.D. & Duvall, A.R. (2018) Multiple paths to straths: A review and reassessment of terrace genesis. *Geomorphology*, 312, 12–23. Available from: <https://doi.org/10.1016/j.geomorph.2018.03.028>
- Sklar, L.S. & Dietrich, W.E. (2001) Sediment and rock strength controls on river incision into bedrock. *Geology*, 29(12), 1087–1090. Available from: [https://doi.org/10.1130/0091-7613\(2001\)029<1087:SARSCO>2.0.CO;2](https://doi.org/10.1130/0091-7613(2001)029<1087:SARSCO>2.0.CO;2)
- Smedley, R.K. & Skirrow, G.K.A. (2020) Luminescence dating in fluvial settings: Overcoming the challenge of partial bleaching. In: Herget, J. & Fontana, A. (Eds.) *Palaeohydrology: Geography of the Physical Environment*. Cham: Springer, pp. 155–168.
- Sohbati, R., Liu, J., Jain, M., Murray, A., Egholm, D., Paris, R. & Guralnik, B. (2018) Centennial- to millennial-scale hard rock erosion rates deduced from luminescence–depth profiles. *Earth and Planetary Science Letters*, 493, 218–230. Available from: <https://doi.org/10.1016/j.epsl.2018.04.017>
- Sohbati, R., Murray, A.S., Chapot, M.S., Jain, M. & Pederson, J. (2012) Optically stimulated luminescence (OSL) as a chronometer for surface exposure dating. *Journal of Geophysical Research: Solid Earth*, 117(B9), B09202. Available from: <https://doi.org/10.1029/2012JB009383>
- Stock, G.M., Ehlers, T.A. & Farley, K.A. (2006) Where does sediment come from? Quantifying catchment erosion with detrital apatite (U–Th)/He thermochronometry. *Geology*, 34(9), 725–728. Available from: <https://doi.org/10.1130/G22592.1>
- Stokes, S., Bray, H.E. & Blum, M.D. (2001) Optical resetting in large drainage basins: Tests of zeroing assumptions using single-aliquot procedures. *Quaternary Science Reviews*, 7(5–9), 879–885. Available from: [https://doi.org/10.1016/S0277-3791\(00\)00045-7](https://doi.org/10.1016/S0277-3791(00)00045-7)
- Thomsen, K.J., Murray, A.S., Jain, M. & Bøtter-Jensen, L. (2008) Laboratory fading rates of various luminescence signals from feldspar-rich sediment extracts. *Radiation Measurements*, 43(9–10), 1474–1486. Available from: <https://doi.org/10.1016/j.radmeas.2008.06.002>
- Whipp, D.M. & Ehlers, T.A. (2019) Quantifying landslide frequency and sediment residence time in the Nepal Himalaya. *Science Advances*, 5(4), eaav3482. Available from: <https://doi.org/10.1126/sciadv.aav3482>
- Wintle, A.G. (1999) AITKEN, M. J. 1998. An Introduction to Optical Dating. The Dating of Quaternary Sediments by the Use of Photon-Stimulated Luminescence. xi + 267 pp. Oxford, New York, Tokyo: Oxford University Press. Price £75.00 (hard covers). ISBN 0 19 854092 2. *Geological Magazine*, 136(1), 83–108. Available from: <https://doi.org/10.1017/S0016756899551777>
- Wintle, A.G. & Murray, A.S. (2006) A review of quartz optically stimulated luminescence characteristics and their relevance in single-aliquot regeneration dating protocols. *Radiation Measurements*, 41(4), 369–391. Available from: <https://doi.org/10.1016/j.radmeas.2005.11.001>
- Wittmann, H. & von Blanckenburg, F. (2016) The geological significance of cosmogenic nuclides in large lowland river basins. *Earth-Science Reviews*, 159, 118–141. Available from: <https://doi.org/10.1016/j.earscirev.2016.06.001>
- Zhang, J.-F., Qiu, W.-L., Wang, X.-Q., Hu, G., Li, R.-Q. & Zhou, L.-P. (2010) Optical dating of a hyperconcentrated flow deposit on a Yellow River terrace in Hukou, Shaanxi, China. *Quaternary Geochronology*, 5(2–3), 194–199. Available from: <https://doi.org/10.1016/j.quageo.2009.05.001>

## SUPPORTING INFORMATION

Additional supporting information may be found in the online version of the article at the publisher's website.

**How to cite this article:** Guyez, A., Bonnet, S., Reimann, T., Carretier, S. & Wallinga, J. (2022) Illuminating past river incision, sediment source and pathways using luminescence signals of individual feldspar grains (Rangitikei River, New Zealand). *Earth Surface Processes and Landforms*, 1–20. Available from: <https://doi.org/10.1002/esp.5357>